Radiation induced defects in quartz and applications to the Arrow uranium deposit in the Athabasca basin, Saskatchewan

A Thesis Submitted to the College of Graduate Studies and Research

In Partial Fulfillment of the Requirements for the Degree of

Master in Sciences in the Department of Geological sciences

University of Saskatchewan

By

Daniele Cerin

PERMISSION TO USE

In presenting this thesis in partial fulfillment of the requirements for a Postgraduate degree from the University of Saskatchewan, I agree that the Libraries of this University may make it freely available for inspection. I further agree that permission for copying of this thesis in any manner, in whole or in part, for scholarly purposes may be granted by the professor or professors who supervised my thesis work or, in their absence, by the Head of the Department or the Dean of the College in which my thesis work was done. It is understood that any copying or publication or use of this thesis or parts thereof for financial gain shall not be allowed without my written permission. It is also understood that due recognition shall be given to me and to the University of Saskatchewan in any scholarly use which may be made of any material in my thesis.

Requests for permission to copy or to make other uses of materials in this thesis in whole or part should be addressed to:

Head of Geological Sciences
114 Science Place
University of Saskatchewan
Saskatoon, Saskatchewan S7N 5E2 Canada

OR

Dean
College of Graduate Studies and Research
University of Saskatchewan
107 Administration Place
Saskatoon, Saskatchewan S7N 5A2 Canada

Abstract

This thesis presents the results of a combined electron paramagnetic resonance (EPR) and cathodoluminescence (CL) study of quartz from the Arrow uranium deposit and its surrounding areas in the southwest margin of the Athabasca basin, Saskatchewan. Detailed EPR analyses of quartz samples from both the basement and the overlying sandstones revealed the presence of a host of different paramagnetic defects (i.e., oxygen vacancy electron centers and silicon vacancy hole centers) previously observed in quartz from the eastern part of the Athabasca basin. The silicon vacancy hole centers were previously shown to have formed from bombardment of alpha particles emitted from the decay series of ^{238}U, ^{235}U and ^{232}Th. Characteristic spectral differences have been observed between quartz from different lithologies, such as the lack of the H_3' centers in basement quartz. Thermal annealing and neutron irradiation experiments suggest that these spectral differences are linked with different diamagnetic precursors, which might be related to growth defects formed during crystallization.

Of the four different types of drusy quartz (translucent, milky, pink and smoky) identified in the basement at the Arrow deposit, only the pink and smoky types contain significant concentrations of paramagnetic defects. Blue quartz in metasedimentary rocks from the basement is characterized by low concentrations of radiation induced defects, suggesting no pervasive uranium-bearing fluids in the basement. Quartz of high EPR intensities is restricted to ~7 m from mineralized areas, confirming the structurally controlled nature of uranium-bearing fluids. CL imaging and spectral analyses also confirmed the EPR results that the translucent and milky types of quartz contain only low levels of radiation induced defects. Smoky quartz with elevated radiation induced defects as revealed by EPR, on the other hand, is characterized by characteristic CL halos and patches associated with uranium-rich minerals and often features well-developed continuous rims, which cross-cut the growth zoning of quartz crystals and apparently suggests remobilization of uranium after quartz crystallization. Pink quartz with elevated radiation induced defects as revealed by EPR does not have the characteristic CL halos, patches or continuous rims, suggesting a homogeneous distribution of radiation induced defects in this type of quartz and pointing to their formation during crystallization from a uranium-bearing fluid. This result, combined with the common occurrence of pink quartz in veins and breccias associated with dravite alteration, suggests that this uranium-bearing fluid might represent the main mineralization event at the Arrow deposit.

The intensities and distribution of alpha-particles-induced defects in detrital quartz close to the sandstone-basement unconformity suggest that uranium-bearing fluids at the Arrow deposit are restricted to the areas immediately above the basement-hosted mineralization. This distribution, together with the low radiation induced defects in detrital quartz, suggests that the basinal fluid along the

sandstone-basement unconformity at the Arrow deposit, if present, was low in uranium, which was mainly transported in basement fluids. The present results further support the suggestion that combined EPR and CL analyses of radiation induced defects in quartz is a powerful tool for the exploration of uranium deposits in the Athabasca basin.

ACKNOWLEDGEMENTS

I would like to thank my supervisor Dr. Pan for the opportunity to work on this project and helping me transition into the fascinating field of geology. I would also like to thank him for his availability to answer my questions, however elementary they might have been, and for his invaluable support and guidance.

I would also like to thank Mr. Garret Ainsworth and Mr. Galen McNamara of NexGen Energy Ltd. for giving me the opportunity to work at Arrow as a student geologist, providing me with all the necessary data to make the most out of this study and patiently answering the multitude of geology related questions I had.

I owe my gratitude to Dr. Ramaswami Sammynaiken of the SSSC (Saskatchewan Structural Science Center) for the precious advice regarding EPR spectroscopy and his help in setting up a variety of different experiments.

I am thankful to the technical staff Mr. Tom Bonli for assisting me in sample analysis.

I would like to express my thanks to Dr. Jens Götze for taking the time to analyze the samples and provide the data without which part of this project would not have been possible.

The funding for this project was provided by NexGen Energy Ltd. in collaboration with NSERC through the engage grant program and the NSERC discovery grant to Dr. Pan.

DEDICATION

I would like to dedicate this thesis to Fizz for always staying by me and giving me the support and motivation to achieve my dreams.

Contents

List of Figures

List of Tables

1 Introduction and objectives

Electron paramagnetic resonance (EPR) spectroscopy is a technique used to study paramagnetic defects with a long standing application in the geological sector, including mineralogy, dating, and the study of radiation induced defects. Initially, radiation damage in quartz was studied with the use of cathodoluminescence (CL) imaging (Morton, 1978). A study conducted by Ramseyer et al. (1988) suggested that the orange-yellow CL colors observed in quartz were caused by lattice damage due to particle bombardment. Several studies observed these distinct yellow-orange CL rims surrounding U or Th inclusions in quartz (Zinkernagel, 1978; Ramseyer et al., 1988; Meunier et al., 1990). These rims were then shown to be caused by α-particles from ^{238}U , ^{235}U and ^{232}Th, with rim thickness consistent with the maximum depth of penetration of α particles emitted during the decay chain of these isotopes (Owen, 1998; Botis, 2005). To enhance this idea Komuro et al. (2002) performed $^{+}$He (4 Mev) implantation on synthetic quartz observing CL haloes of the same wavelength as those found in irradiated natural quartz and confirming predicted rim width. The paramagnetic defects associated with these CL rims have been the subject of numerous studies. The most well characterized of these defects are the electron-like centers which are related to a missing oxygen atom and can be induced by diverse radiation energies/sources (e.g., X- and γ-rays; Weeks, 1956; Silsbee, 1961; Weil, 1984; Boero et al., 1997) . Irradiated quartz also possesses a variety of hole-like centers which are related to a missing silicon atom and are formed from bombardments of α and β particles emitted from radioactive decays of heavy isotopes such as U and Th (Mashkovtsev et al., 1978; Botis et al., 2008; Hu et al. 2008; Pan et al., 2008).

Hu et al. (2008) applied EPR spectroscopy in parallel with CL analysis to study quartz grains from the Athabasca basin confirming high concentration of Si vacancy centers in the CL rims. The literature is in good agreement that EPR provides a much more sensitive analysis of radiation-induced defects (RIDs), making this technique promising in the exploration of U deposits in the Athabasca region and other areas of economic interest for U deposits. For example, quartz grains in mineralized samples (Cigar Lake, Key Lake, and McArthur River) contain extremely high levels of these hole-like centers. Also, quartz grains in sandstones along the unconformity with the basement in different parts of the Wheeler River property contain highly variable levels (i.e., by more than two orders of magnitudes) of these hole-like centers, which have been interpreted to record the presence and absence of uranium-bearing fluids. In addition, quartz in non-radioactive druses up to 400 meters above the orebodies at the McArthur River deposit contains elevated levels of hole-like centers, interpreted to record the formation of these druses from uranium-bearing fluids. These results demonstrate that these alpha-particles-induced hole-like centers in quartz from the eastern part of the Athabasca basin are useful

for not only detecting the past presence of uranium-bearing fluids but also possibly tracing the direction of uranium-bearing fluid flows in the basin.

Several discoveries of significant uranium mineralization (e.g., the Triple R deposit and the Arrow deposit) have recently been made in the south-western Athabasca Basin. These new uranium deposits, different from their eastern counterparts (e.g., Cigar Lake, Key Lake and McArthur River deposits) in close proximity to the Athabasca sandstone-Precambrian basement unconformity (Jefferson et al., 2007), occur almost exclusively in the basement. One immediate question is whether most of the exploration strategies developed for the eastern Athabasca Basin are applicable to the south-western part of this basin or not. For example, delineation of uranium-bearing fluid flows is of importance to all uranium exploration programs. Mineralization fluids in the unconformity-hosted uranium deposits in the eastern Athabasca basin have been suggested to focus mainly along the sandstone-basement unconformity, but are expected to be more difficult to identify and trace in basement lithologies owing to complex lithologies and structures.

1.1 Research objectives

This thesis reports the results from the study of radiation induced defects in quartz from the Arrow uranium deposit in the Athabasca basin. The main purpose of this thesis is to study the association between radiation defects and different quartz types identified in the region and how they are related to mineralization fluids. Particular interest was also placed in comparing obtained data with previous studies in the eastern Athabasca basin and evaluate if observed trends continue at the Arrow deposit or if significant differences are present. The principal technique used to study the radiation induced defects is electron paramagnetic resonance whose sensitivity (more than 10000 times that of optical resonance spectroscopy; Weil, 1984) makes it the preferred method for observing the centers of interest. Selected samples were also observed with CL spectroscopy and microscopy in order to study the distribution of the defects in the grains and crystals and to acquire more information on the timing of the U-events in relation to quartz growth.

1.2 Chapter description

Chapter 2 deals with the fundamental physics behind EPR spectroscopy and the paramagentic lattice defects of interest in quartz.

The following chapter provides a brief overview of previous literature on the subject that was the basis for this project. It focuses on previous CL and EPR studies of Athabasca quartz: concentration of defects in relation to lithology, correlation between CL rims and EPR spectra and relation between uranium and observed defects.

Chapters 4 provides a brief overview of the Athabasca basin geology and a more detailed look at the Arrow area and the deposit with particular attention to the different

quartz types found in the basement.

Chapter 5 explains sampling procedures and criteria as well as detailing their preparation it also lists the experimental parameters used in this study and in all presented spectra throughout this thesis.

Chapter 6 presents the data obtained from sample analysis and how it relates to quartz events in the area. Results on EPR spectra, defect intensity distribution (in both sandstone and basement) and CL analysis are all presented in this section. CL data presented in this section was collected by Prof. Jens Götze at the TU Bergakademie Freiberg.

2 Electron Paramagnetic Resonance spectroscopy

Electron paramagnetic resonance (EPR) spectroscopy, also known as electron spin resonance (ESR) spectroscopy,), is a widely used spectroscopic technique to study paramagnetic centers. The principles of EPR spectroscopy closely resemble the ones of NMR spectroscopy, however instead of exciting nuclear spins, in the former unpaired electronic spins are excited. This technique provides a host of information about the structure of the species studied; in addition quantitative EPR studies can be useful for chemical analysis, dosimetry and geochronology. EPR spectroscopy is known for its greater sensitivity (10^{12} spins/cm^3 or parts per billion) over other techniques in detecting and characterizing dilute paramagnetic species in various hosts (Calas, 1988; Weil and Bolton, 2007; Pan et al., 2002). However, even though applications of EPR to geology and Earth science have been varied, its use has been limited due to the lack of knowledge surrounding many paramagnetic defects, and the preference of other, simpler and more accessible, techniques. For example despite numerous investigations being conducted on the structure and occurrence of paramagnetic defects in quartz, there remains a lack of understanding as some of these defects are still poorly characterized and not well understood. Paramagnetic quartz defects are of particular importance due to their connection with absorbed radiation, their stability in regards to time, and the high temperatures required to anneal them.

2.1 Physics of EPR spectroscopy

This method is a way of observing the resonance absorption of microwave radiation by paramagnetic structures in an applied magnetic field. States that can be analyzed with this technique include: transition metal ions, point defects in solids, free radicals in a variety of different states, systems with multiple unpaired electrons and with conductive electrons (metals and semiconductors). EPR has seen extensive use in the fields of chemistry, biochemistry, medicine, physics and in geological sciences.

Fundamental principles An electron is a subatomic particle (lepton) with a negative elementary electric charge, it possesses an intrinsic spin momentum S with module:

$$|\vec{S}| = \sqrt{S(S+1)}\hbar \tag{1}$$

and z component:

$$S_z = m\hbar \tag{2}$$

with m assuming values S, S-1, S-2, ..., -S. Consequently, electrons can possess two possible values $m = \frac{1}{2}, -\frac{1}{2}$. The electron, being a charged particle also also has a magnetic momentum, causing the electron to orientate in two opposing direction under the effect of an external magnetic field. That creates the following energy levels directed along the z axis (free electron; Figure 1):

$$E = g_e \beta_{\mathrm{e}} m B_0 \tag{3}$$

with $g_e (= 2.0023193)$ being the gyromagnetic factor of the free electron and β_{e} being the Bohr magnetron. Furthermore the energy difference between the lower excitation level and the higher is

$$\Delta E = h\nu \tag{4}$$

where h is the Planck constant and ν is the excitation frequency. As a result, When this condition is met absorption occurs and is measured in the experiment. A more complex EPR experiment where the electron is interacting with surrounding nuclei and other electrons can be described by an appropriate spin Hamiltonian [**?**, 53, **?**]:

$$\begin{aligned}
\mathcal{H}_{\mathcal{N}} = {} & \beta_{\mathrm{e}} S_N^T \cdot \mathrm{g} \cdot \mathrm{B}_N + S_N^T \cdot D \cdot S_N + \\
& \sum_{\alpha=2}^{\mathrm{Nspins}} \Big[(S_N^T \cdot^{\alpha} A \cdot^{\alpha} I_N - \beta_n^{\alpha} I_N^T \cdot^{\alpha} g_n \cdot B_N +^{\alpha} I_N^T \cdot^{\alpha} P \cdot^{\alpha} I_N) + \\
& \sum_{\alpha'=\alpha}^{Nspins} \frac{(^{\alpha} I_N^T \cdot^{\alpha\alpha'} J \cdot^{\alpha} I_N +^{\alpha} I_N^T \cdot^{\alpha\alpha'} J \cdot^{\alpha} I_N)}{2} \Big] + \\
& \textit{other high spin terms such as } BS^3, S^4, BS^5, S^6, SI^3, SI^5, S^3I, S^5I, I^4, I^6, ...
\end{aligned} \tag{5}$$

Where N spins is the number of nuclear spins , β_N is the nuclear magnetron , ${}^{\alpha}g_n$ is the nuclear gyromagnetic factor, ${}^{11}J = D$ and ${}^{1\alpha}J = {}^{\alpha} A$.

The first term of the equation describes the Zeeman interaction between the field and the magnetic moment of the electron, g is a 3x3 tensor whose eigenvalues correspond to the energy levels. This matrix may be diagonalized by selecting an appropriate coordinate system, the values g_{11} , g_{22} , g_{33} (i.e. $g_{max}, g_{int}, g_{min}$) obtained are called the principal values (McGavin, 1987). The second term (S^2) represents the zero-field interaction reflecting the strong dipole-dipole interactions between the electrons. Another important term is the one representing the hyperfine interaction (SI) between the electron's angular momentum and the nuclear spin, further splitting may occur if the electron is subject to the influence of multiple sets of equivalent nuclei. Other terms are the nuclear zeeman term (BI) for the nuclei with non-zero spin (I) and the nuclear quadrupole (I^2) arising from the interaction of the electric quadrupole moment of these nuclei with the electric field gradient. Remaining term include the interelectronic coupling with other unpaired electrons (S_1S_2), internuclear coupling of multiple non-zero spin nuclei (I_1I_2), fourth degree fine structure (S^4), nuclear octupole (I^4), other higher order and generally not as

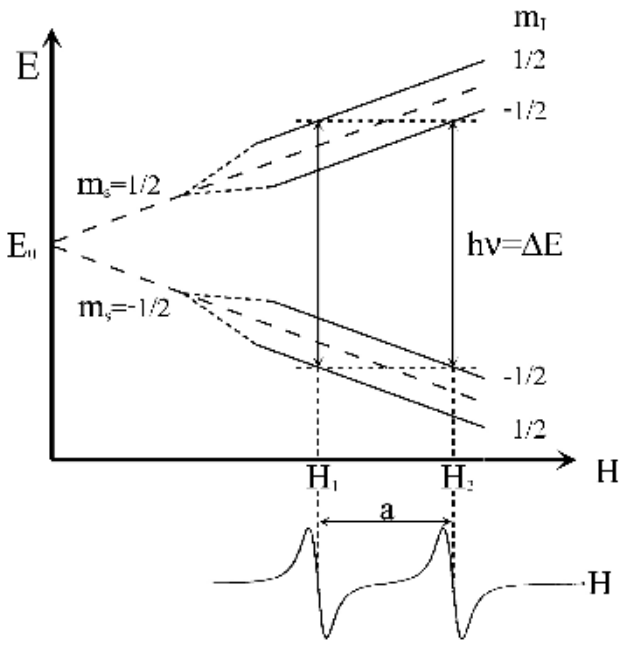

Figure 1: Energy levels of a radical with a nucleus with I = 1/2 and its corresponding EPR spectrum.

significant orders of interaction.

It is evident that a well resolved EPR spectra provides substantial information regarding the paramagnetic species: from electronic structure to site occupancy, symmetry of the sites, nature of neighboring atoms, site concentration and other related data. While orientation is an important factor when analyzing single crystals, when using powdered samples, questions related to symmetry-related sites can be ignored due to spatial averaging (Figure 2). The EPR spectra is the average of all the possible orientations; in such an experiment three principal g-factor values (g_1 or g-maximum, g_2 or g-intermediate, and g_3 or g-minimum) are used to describe a specific species (Rae, 1969), although when considering isotropic and axial species there is need of only one for the former and two principal values for the latter. Figure 3 shows typical lineshapes for powdered samples. Another parameter affecting the obtained spectra is the concentration of the paramagnetic species studied and the relative population of the excited and base states. The population ratio is determined by the Boltzmann distribution law:

$$\frac{n_e}{n_g} = e^{-\frac{g\mu B}{k_b T}} \tag{6}$$

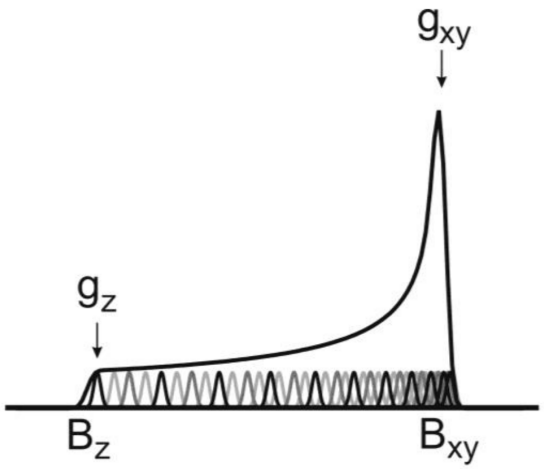

Figure 2: Cumulative peak observed in powder spectra originated from the sum of peaks in all possible directions

with n_e being the number of spins in the excited state and n_g the ones in the ground state. This means that a decrease in temperature and increasing the microwave frequency are two ways of increasing the population difference and thus the sensitivity. Theoretically speaking, the sensitivity of spectrometer with increased microwave frequency shoulder be greater. However, since the higher frequency waveguides are smaller, samples are necessarily smaller, thus canceling the advantage of a more favorable Boltzmann factor.

Linewidth is also an important parameter in an EPR spectrum. In some cases multiple peaks (for example due to hyperfine interaction) with small distance between each other can appear as a singular peak. Linewidth is affected by spin-lattice and spin-spin relaxation times; the former is determined by the energy dissipation via thermal vibrations of the lattice and is reduced at low temperatures. The latter is influenced by dipolar and exchange interactions of proximal spins and is temperature independent , it is lower in dilute samples.

The last important parameter is the frequency of the microwaves used to excite the electrons of the sample. Since the intensity of the magnetic field is variable a host of different frequencies are available to be used, the most common are X-band, S, K, Q, W. By far the most common is X-band since it provides the most optimal sensitivity but recently higher energy frequency machines have become more widely used.

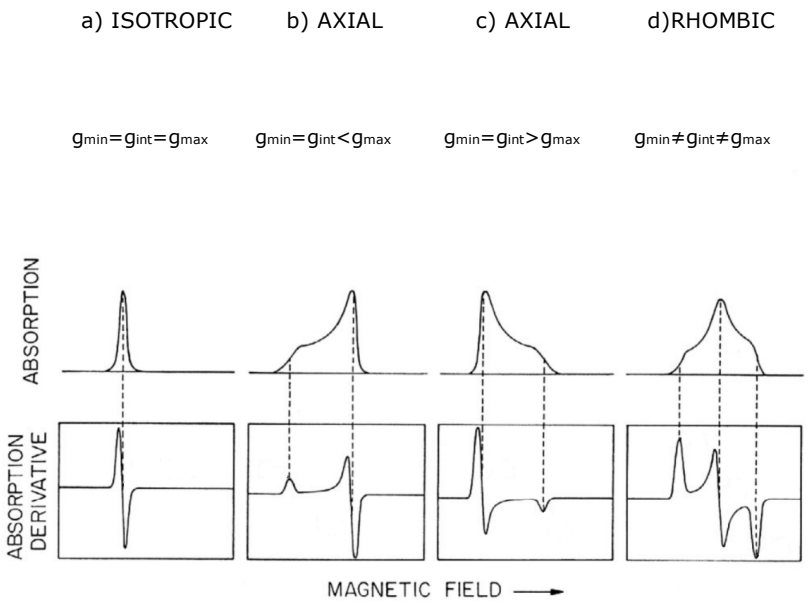

Figure 3: Lineshapes and absorption spectra for centers of different g-values (Modified from Duin, digital document)

Letter Designation	Frequency Range
L Band	1-2 GHz
S Band	2-4 GHz
C Band	4-8 GHz
X Band	8-12 GHz
Ku Band	12-18 GHz
K Band	18-26.5 GHz
Ka Band	26.5-40 GHz
Q Band	30-50 GHz
U Band	40-60 GHz
V Band	50-75 GHz
E Band	60-90 GHz
W Band	75-110 GHz
F Band	90-140 GHz
D Band	110-170 GHz

Different experimental setups allow the observation of different transitions that are hidden at one applied field strength, but clearly visible at another. This is because at a higher magnetic field strength, the spin states will be split further, spreading apart transitions that are close in energy.

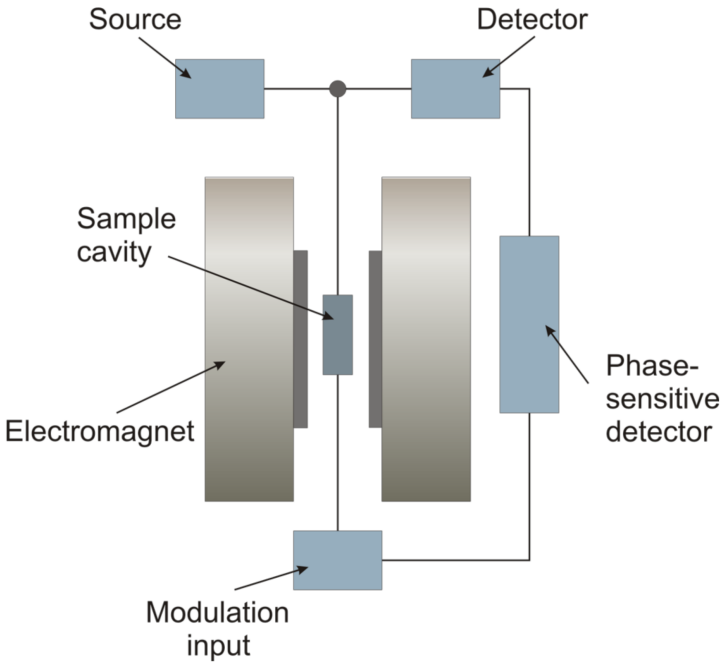

Figure 4: Schematics of an EPR spectrometer

2.2 EPR spectrometer

The basic setup of an EPR spectrometer (Weil, 1984) consists of an electromagnetic wave generator, a resonant cavity, a pair of magnets, a detector and a computer for acquiring the data. Most experiments are done at a fixed microwave frequency and the magnetic field is varied although in some machines frequency may be varied and the field kept constant. The source produces radiation in the microwave region as such frequencies are required to induce resonance transitions under the produced magnetic fields. The source is usually a klystron vacuum tube known to be stable, high power microwave sources that have low-noise characteristics and thus give high sensitivity. The sample is placed in a resonant cavity which admits microwaves through an iris. The cavity is located in the middle of an electromagnet and helps to amplify the weak signals from the sample. Most of the external components, such as the source and detector, are contained within a microwave bridge control. Additionally, other components, such as an attenuator, field modulator, and amplifier, are also included to enhance the performance of the instrument.

In EPR spectrometers, a phase-sensitive detector (or lock-in amplifier) is used. This allows for weak signal recovery from what would normally be buried under higher intensity noise. This is done by using a reference signal and multiplying it by the input and then integrating it over a specific amount of time. In the resulting signal, the contribution from any signal that is not at the same frequency as the reference signal is attenuated close to zero. This results in the absorption signal being presented as the first derivative.

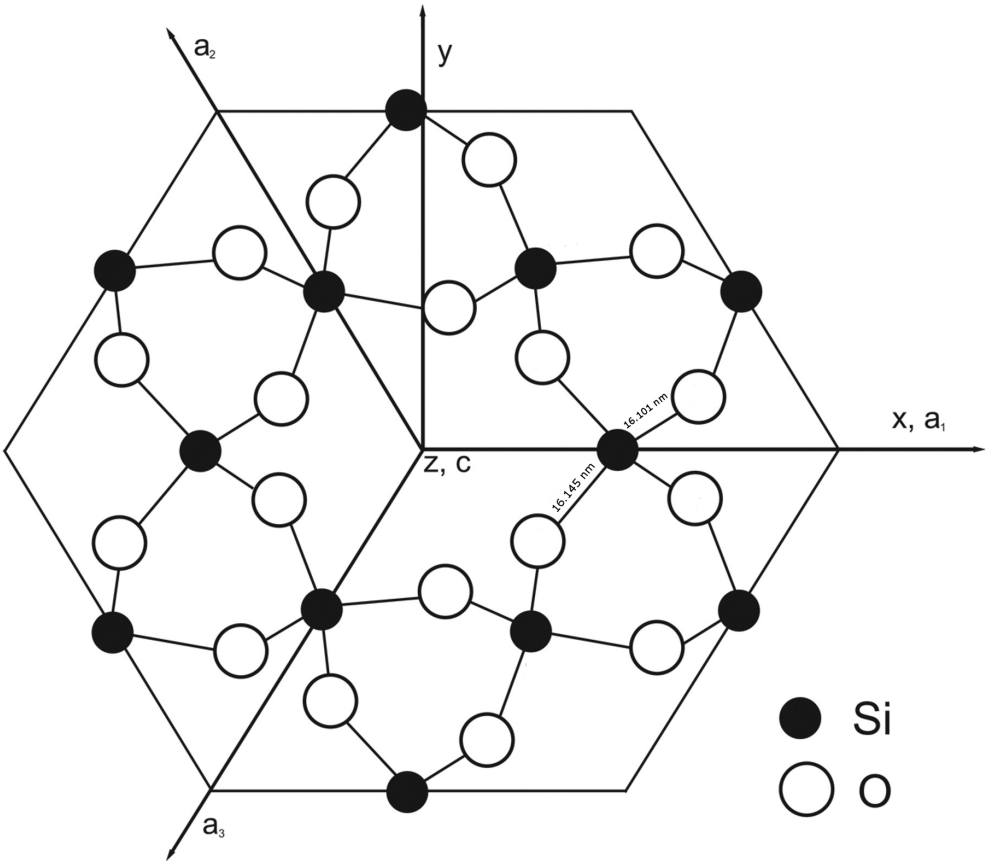

Figure 5: Quartz crystal structure projected on the plane perpendicular to the c-axis. The hexagonal cell unit and its 3 identical (a_1, a_2, a_3) axes are shown as well as the location of the Si atoms on the axes.

2.3 Paramagnetic defects in quartz

2.3.1 Quartz structure

In quartz each Si atom is bonded to four oxygen ones and each oxygen atom to two Si. Quartz is divided into α-quartz and β-quartz; the former has a trigonal crystal structure with space groups $P3_121$ and$P3_221$ while the latter is part of the hexagonal system with space groups $P6_222$ and $P6_422$. In either case, no center or plane of symmetry is present. Considering the hexagonal cell unit, four axes are used as a reference system. Axes a_1 and a_2 and a_3 are at a 120° angle to each other and coincide with the C_2 symmetry axes. The fourth axis (Figure 5) coincides with the crystallographic c axis and is normal to the plane identified by a_1 and a_2. In quartz there are 3 Si and 6 O atoms in the unit cell, Si_3O_6.

The SiO_4 deviates from a perfect tetrahedron because of non-uniform bond length between the silicon and oxygen atoms. Two bonds , called "long bonds", measure about 16.145nm (94K) while the other two short bonds, measure 16.101 nm (94K) (LePage et al., 1980). These units occur in 3 different orientations in the crystal structure connected to each other by rotations along the c axis. Crystal structure consists of one big c-axis

Table 1: **Spin-Hamiltonian parameters of E_1' defect**

	parameters		$\theta(^\circ)$	$\phi(^\circ)$		$\theta(^\circ)$	$\phi(^\circ)$
	Right	handed			Left	handed	
g	g_1	2.00176	66	230	2.00179	114.5	227.7
	g_2	2.0049	52	339	2.00053	134.5	344.4
	g_3	2.0029	45	114	2.00030	125.4	118.7

channel surrounded by 6 parallel smaller channels. These large c-axis channels provide a good location for the interstitial cations, which can diffuse along the channels.

2.3.2 Defects in quartz

Quartz defects can be categorized into 3 main categories: point defects, translations and inclusions (Figure 6; Gotze at al., 2001). The type and abundance of defects is influenced by the thermodynamic conditions during crystallization. During quartz crystallization impurites and lattice defects are created as charge compensated diamagnetic defects who may be afterwards transformed into paramagnetic centers by natural or artificial irradiation.

Paramagnetic vacancy centers Paramagnetic defects can be subdivided into 2 main types: those associated with foreign ions and centers associated with oxygen (electron-like centers) or silicon vacancies (hole-like centers). Oxygen vacancy centers are divided into E' and E" to denote one or two trapped electrons and have subscript numbers between 1-10 to indicate different electron trappings. The E_1' defect (Table 1) is the most common in quartz and the most well characterized (Alessi et al., 2014). This defect consists of an electron in an oxygen vacancy, where the electron occupies a dangling sp3 hybrid orbital of silicon bonded to three oxygen atoms (Botis, 2005). The E_1' center can be produced and observed at room temperature by means of γ, electron or neutron irradiation of quartz. The E_1' defect increases in intensity with temperature up to 200°C and is annealed out between 360-380°C (Ikeya, 1993; Pan and Hu, 2009). In hole-like centers instead (Table 2), the absence of a Si atom in the lattice can lead to hole trapping by two or three oxygen ions and the formation of O_2^{3-} superoxide (O_2^-), ozonide (O_3^-) and peroxide radicals ($\equiv Si - O - O\bullet$) (Azzoni et al., 1994).

Impurity centers Impurity ions are also present by substituting Si atoms in the lattice. Typically these atoms are Al^{3+}, Ge^{4+}, P^{5-}, Fe^{3+} , Ga^{3+} or Ti^{4+} (Gotze at al., 2001; Weil, 1984). These ions occupy either substitutional or interstitial positions in the quartz

Table 2: **Spin-Hamiltonian parameters of silicon vacancy centers**

T(K)	g_k	$\theta(\cdot)$	$\phi(\cdot)$	nuclei	A_k(mT)	$\theta(\cdot)$	$\phi(\cdot)$
#1 / H_1'	2.02945	26	266.2	^{27}Al	0.024	79	352
Nilges et al., 2009	2.00765	64	91.2		-0.025	63	87
	2.00210	88	0.3		-0.027	29	242
B / H_2'(I)	2.03505	22.1	172.6	^{27}Al	-0.222	65	156
Pan et al., 2008	2.00773	71.1	319.3		-0.292	42	36
	2.00234	78.6	5.32		-0.3	58	263
B' H_2'(II)	2.03555	22.1	165.5	^{27}Al	-0.27	62	156
Pan et al., 2008	2.00771	69.5	319.5		-0.35	107	237
	2.00231	80.9	52.9		-0.36	33	300
D H_3'(I)	2.04953	73.6	2.48.9	^{27}Al	-0.038	73	28
Pan et al., 2009	2.00701	50.1	353		-0.14	77	122
	2.00206	44.4	141.5		-0.146	20	248
E / H_3'(II)	2.05175	76.4	244.1	^{27}Al	-0.020	51	302
Pan et al., 2009	2.00682	51.7	345.1		-0.092	38	128
	2.00213	41.5	138.2		-0.101	92	214
G / H_4'(I)	2.03079	46.3	1.5	^{27}Al	-0.306	57	303
Nilges et al., 2008	2.00816	84.2	266		-0.306	57	303
	2.00226	44.2	170.1		-0.421	72	45
G' / H_4'(II)	2.02918	46.7	1.2	^{27}Al	-0.41	54	309
Pan et al., 2008	2.00828	84.6	266.1		-0.51	39	159
	2.00229	43.7	170.5		-0.54	74	50
C / H_7'(I)	2.0183	36.7	270	^{27}Al	0.15	33	90
Maschmeyer and	2.0090	90	0		0.121		
Lehmann, 1983	2.00248	63.3	90		0.12		
C' / H_7'(II)	2.01698	30.7	274.9	^{27}Al	-0.1	53	309
Pan et al., 2008	2.00823	75.2	158.6		-0.21	57	191
	2.00248	63.7	61.1		-0.22	52	72
#3	2.0056	90	0				
Azzoni et al., 1994	2.0044	54	90				
	2.0008	36	270				

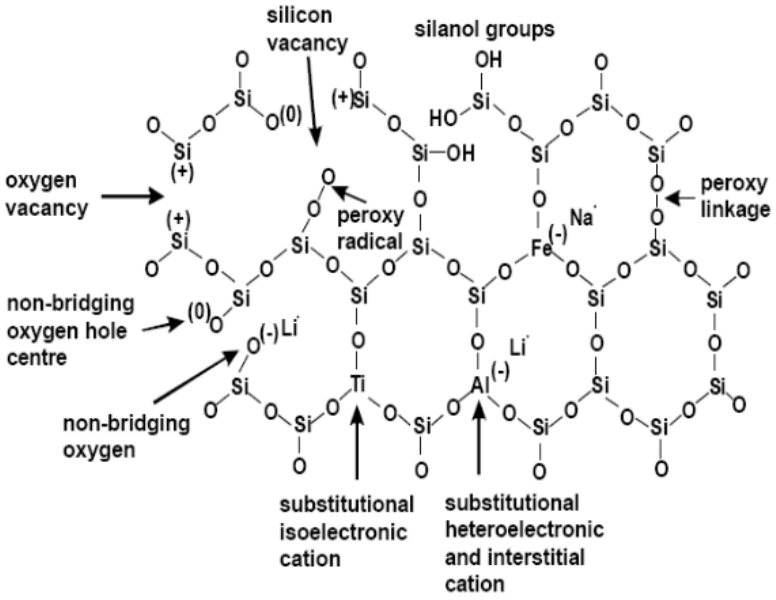

Figure 6: Common defects found in quartz lattice (Gotze et al. 2001)

lattice depending on ion radius and charge. The number of ions, which can substitute for the silicon atom in the quartz lattice, is limited because of the small ionic radius of Si^{4+} (0.42Å) compared to its high valence. Since, in the case of some ions, compensation of the electric charge is necessary, additional cations such as H^+, Na^+, K^+, Li^+, Fe^{2+}, Cu^+, Co^{2+} or Ag^+ can be incorporated inside the previously mentioned large open channels that run parallel to the c-axis (Figure 6). Due to very similar atomic sizes Al^{3+} easily substitutes for a Si^{4+} atom in the lattice and is the most prevalent impurity in quartz.

3 EPR-CL studies of quartz in the Athabasca basin

In previous studies the presence of RIDs in quartz was associated with uranium mineralization and U-bearing fluids. These silicon vacancy RIDs are known to be characteristic of bombardment by α particles derived from the decay U decay chain (Meunier et al., 1990; Komuro et al., 2002; Botis et al., 2005; Botis et al., 2006). Initially these defects were observed and studied in Athabasca quartz by means of CL imaging and spectroscopy but EPR was shown to have more potential due to its superior sensitivity in detecting dilute paramagnetic species (Morton, 1978; Botis, 2005).

Previous studies of quartz from the Athabasca basin analyzed samples from multiple different locations in the eastern basin, such as: McArthur River, Mann Lake, Cree extension, Maw zone and Key Lake. Samples were mainly collected from the Athabasca sandstone (both drusy and detrital), near the unconformity and more altered areas, and in a lesser amount in the crystalline basement. Analysis of the quartz grains revealed continuous yellow orange CL rims and patches that were associated with bombardment by alpha particles (Owens, 1998), three different types of radiation related CL patterns were identified (Botis et al., 2005). The first type can be observed as concentric haloes around U or Th bearing minerals; the second appears as patches along quartz grains near α-radioactive minerals inside matrices or pores; type three as continuous rims in contact or not with U bearing minerals (Figure 7a). These CL haloes were more intense in association with uraninite (in comparison to other uranium bearing minerals in the sandstone) that suggests a direct relationship between intensity of CL emissions and radiation dose the grain was subjected to. It's of interest to note that in the case of CL patches surrounding inclusions, those are directly associated with U-bearing minerals and can be found in sandstone from almost any location and depth. Conversely the continuous rims are not only seen in mineralized and alteration halo around deposits, but are also observed in grains not in contact with radioactive minerals. The location of CL patches and rims in drusy grains was also shown as a source of information about the timing of the uraniferous fluids and their relation with quartz growth (Botis et al., 2006). EPR analysis corroborates the data obtained from CL of the quartz grains (Figures 7a and 7b compare CL emissions and EPR spectra from the same sample), confirming the presence of peroxy radicals and oxygen vacancy defects associated with alpha particle bombardment in samples that exhibited yellow-orange CL colors.

Powdered EPR of drusy quartz in previous studies (Botis et al., 2008, Hu et al., 2008) revealed mainly the presence of a host of different paramagnetic defects (including #1, E_1',B,B',C',D,E,G) some of which were previously not thought to occur in naturally irradiated quartz but were observed in artificially irradiated crystals (Mashkovtsev et al., 1978, Maschmeyer and Lehmann, 1983). The same centers were observed in detrital

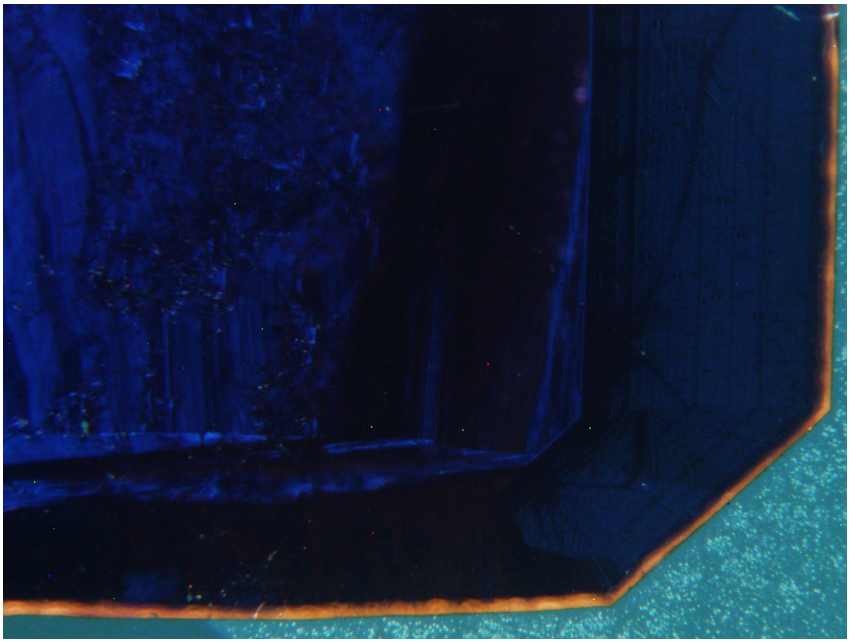

(a)

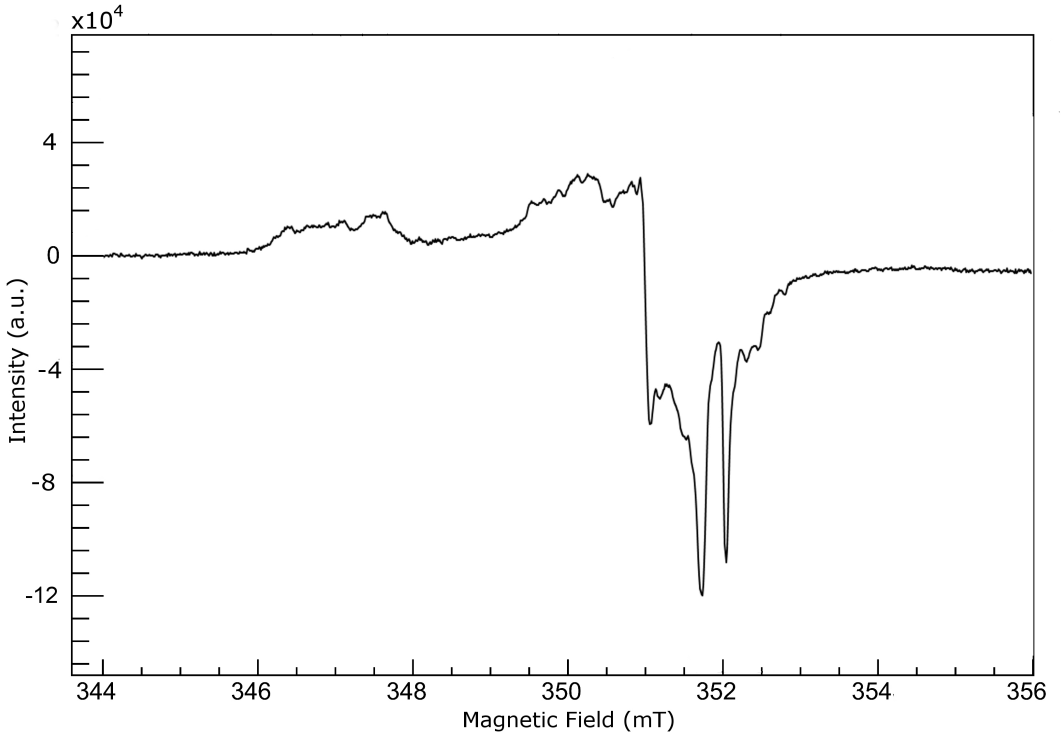

(b)

Figure 7: Comparison of CL image and EPR spectra of drusy smoky quartz from sample 5711425, note the characteristic yellow-orange rims caused by alpha particle damage.

quartz apart from B and B'. Alessi et al. (2014) reviewed these hole-like centers in quartz and, by analogy with their electron-like counterparts, recommended a new nomenclature (i.e., H_1' to H_7') to avoid the random names adopted in the literature.

While most of the observed defects were shown to be correlated to alpha particle damage, center E_1' is found in grains near and far from U or Th rich minerals and its distribution does not correspond with the shallow penetration power of alpha radiation but rather with gamma radiation; it is thus not a good indicator for the presence , or past occurrence, of U bearing fluids in the area. The E_1' center has though been proposed as a means of dating the quartz by comparing its intensity to the estimated rate of radiation it was subjected to (Toyoda at al., 1998) High concentrations of RIDs were found to be present at lithological boundaries, near U- or Th- bearing minerals and near the unconformity. In the basement rocks below mineralization the defects were found to be below detection suggesting U-deficency in the basement fluids. Generally RID intensity were observed to increase from the surface to the unconformity and in the alteration haloes but they are still detectable in non-altered shallow sandstone albeit with lower intensity (Botis et al., 2006). The higher intensity of centers in some samples of drusy quartz compared to detrital samples, with similar U and Th amounts, suggests the presence of ancient U-bearing fluids that flowed through the fractures and cavity during the formation of the drusy quartz (Hu et al., 2008). As further confirmation, hydrofluoric acid treatment of samples showed a marked decrease of peak intensity below the calculated one due to mass loss. This suggests that the defects were concentrated on the outer rims of the quartz crystals and were caused by the presence of the aforementioned U-bearing fluids through the rock. However in some detrital quartz grains this difference isn't noticed indicating that the defects may be due to the presence of uranium bearing mineral inclusions that are distributed randomly throughout the quartz volume, thus not being reduced preferentially by hydrofluoric acid treatment.

Studies were also conducted in non-mineralized areas (such as the Maw zone) where the drusy quartz from the basement and the sandstone was found to be deficient in RIDs (Pan et al., 2013), and when they were present the intensities were an order of magnitude below the ones in altered sandstone from areas of known mineralization (such as Key Lake and McArthur River). This shows the possibility of using EPR spectroscopy for discerning barren or mineralized areas, since the haloes of intensely altered rock that surround known deposits are present even in areas lacking U-bearing fluids, such as the Maw zone.

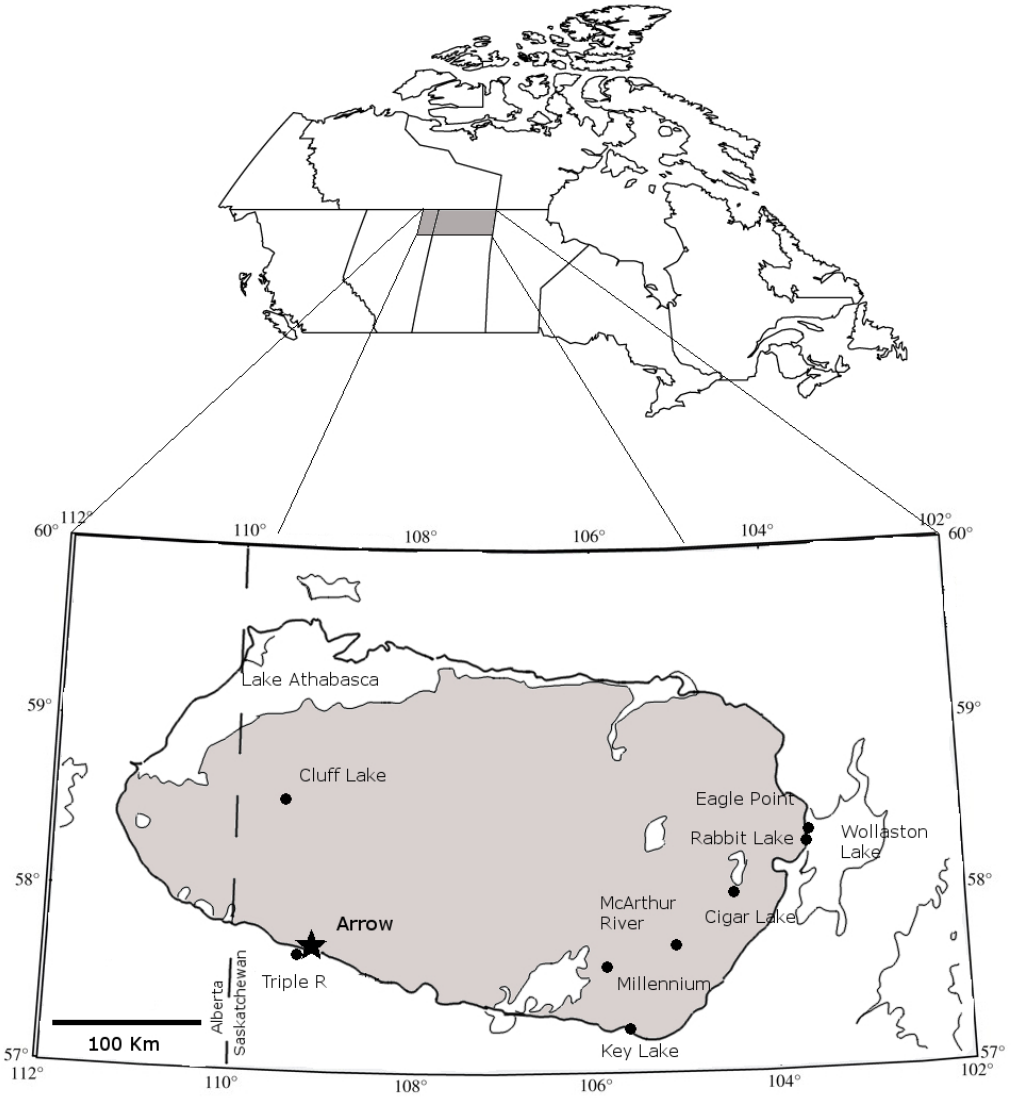

Figure 8: Location map showing the Arrow and Triple R deposits in the south-western margin of the Athabasca Basin, Saskatchewan, Canada.

4 Geology

4.1 Athabasca Basin Geology

The Eastern Athabasca Basin is characterized by Late Paleo- to Mesoproterozoic sandstones and conglomerates overlying Archean granitic gneisses and Paleoproterozoic metasedimentary rocks, and hosts world class uranium deposits (e.g., Cigar Lake, Key Lake and McArthur River deposits; Jefferson et al., 2007; Yeo et al., 2007; Pan et al., 2013). The sedimentary units, from oldest to youngest, in the Athabasca Basin are divided into the Fair Point, Smart and Read, Manitou Falls, Lazenby Lake, Wolverine Point, Locker Lake,

Otherside, Douglas, and Carswell formations (Ramaekers et al., 2007; Yeo et al., 2007). Most of the uranium deposits are located in the eastern part of the Athabasca basin and have been classified into two distinct types: one usually situated at the intersections of the sandstone–basement unconformity and faults (Hoeve and Sibbald, 1978; Jefferson et al., 2007; Li et al., 2016) and characterized by the presence of abundant Ni–Co–As–Fe–Cu–Pb sulfides and arsenides; and another confined entirely in faults and fractures in basement rocks and characterized by a general lack of sulfides and arsenides.

4.2 Local Geology

The Arrow and Triple R deposits are two recent discoveries of uranium mineralization located just inside the south-western margin of the Athabasca basin (Figure 8). The area is defined by a gravity low (interpreted to arise from intense clay alteration of basement rocks) and by a disrupted EM conductor (NexGen presentation, 2015; Mathisen and Ross, 2016).

At the Arrow deposit the topmost 40-80m strata are Quaternary glacial tills (Figure 10a) and cretaceous sediments of mainly of mudstone and siltstone (Figure 10b) and Devonian green-gray clay (Figure 10c). The underlying Athabasca sandstone and conglomerate (Figure 10d) that is part of the Manitou Falls formation overlies the unconformity, its thickness varies between 5-30 m and thins to the southwest. Therefore the sandstone-basement unconformity at Arrow is found on average at the depth of 100 meters, and is underlain by a paleoweathering profile that can be divided into an upper bleached zone and a lower hematite-rich zone. The paleoweathering profile is cut and affected by later structures and hydrothermal fluids. The basement underneath the paleoweathering profile is composed mainly of pelitic to semi-pelitic gneiss and granofels (Figure 10e, f, g, h), and is crisscrossed by a series of NE-SW trending graphitic structures such as shears and mylonites (Figure 10i), which extend almost vertically from the unconformity to unknown depth. An intrusive package of mainly granodioritic gneiss and gabbro (Figure 11a,b) is present in the basement as well as the local presence of smaller assemblages of pegmatites and garnetites (Figure 11c, d) (NexGen presentation, 2014; Hillacre, 2015; Mathisen and Ross, 2016)

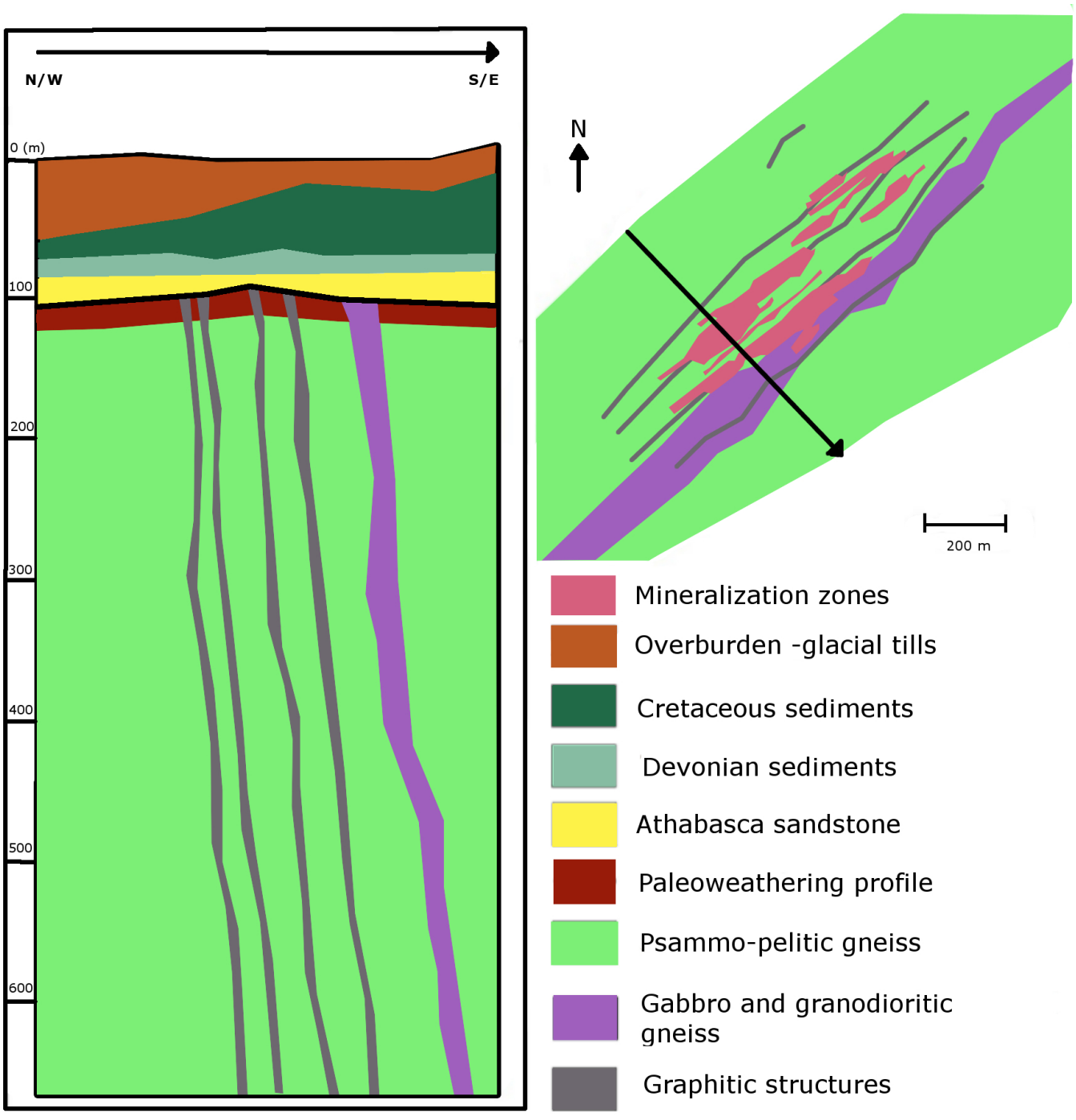

Figure 9: Cross section showing major lithologies at the Arrow deposit and basement geology projected to the unconformity (Modified from Mathisen and Ross, 2016; NexGen presentation, 2015; NexGen presentation, 2014).

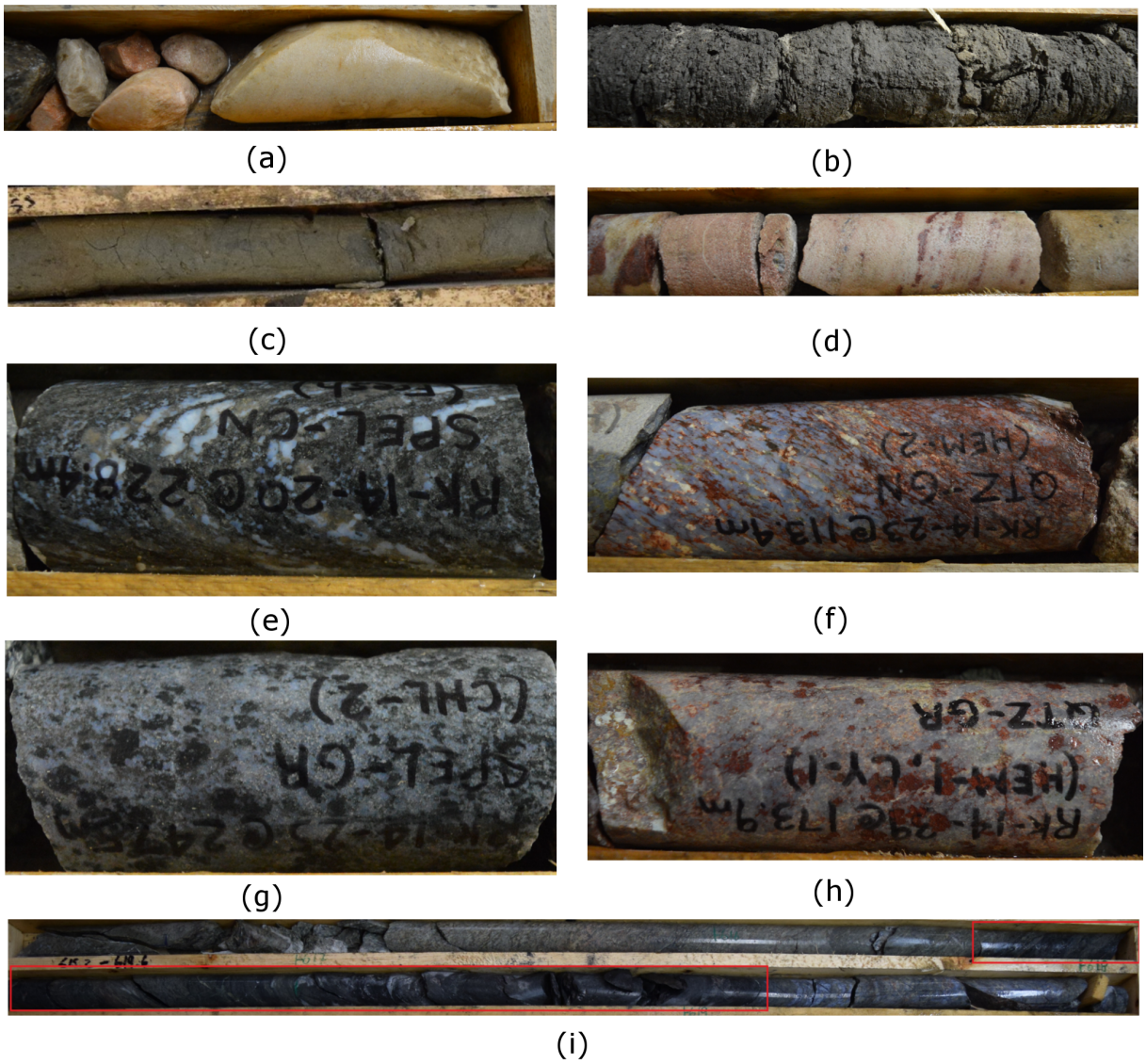

Figure 10: a) Glacial till. b) Cretaceous mudstone and siltstone. c) Devonian clay. d) Athabasca sandstone and conglomerate. e) Semi-pelitic gneiss. f) Quartz-rich semi-pelic gneiss. g) Semi-pelitic granofels. h) Quartz-rich semi-pelitic granofels. i) Graphitic shear zone.

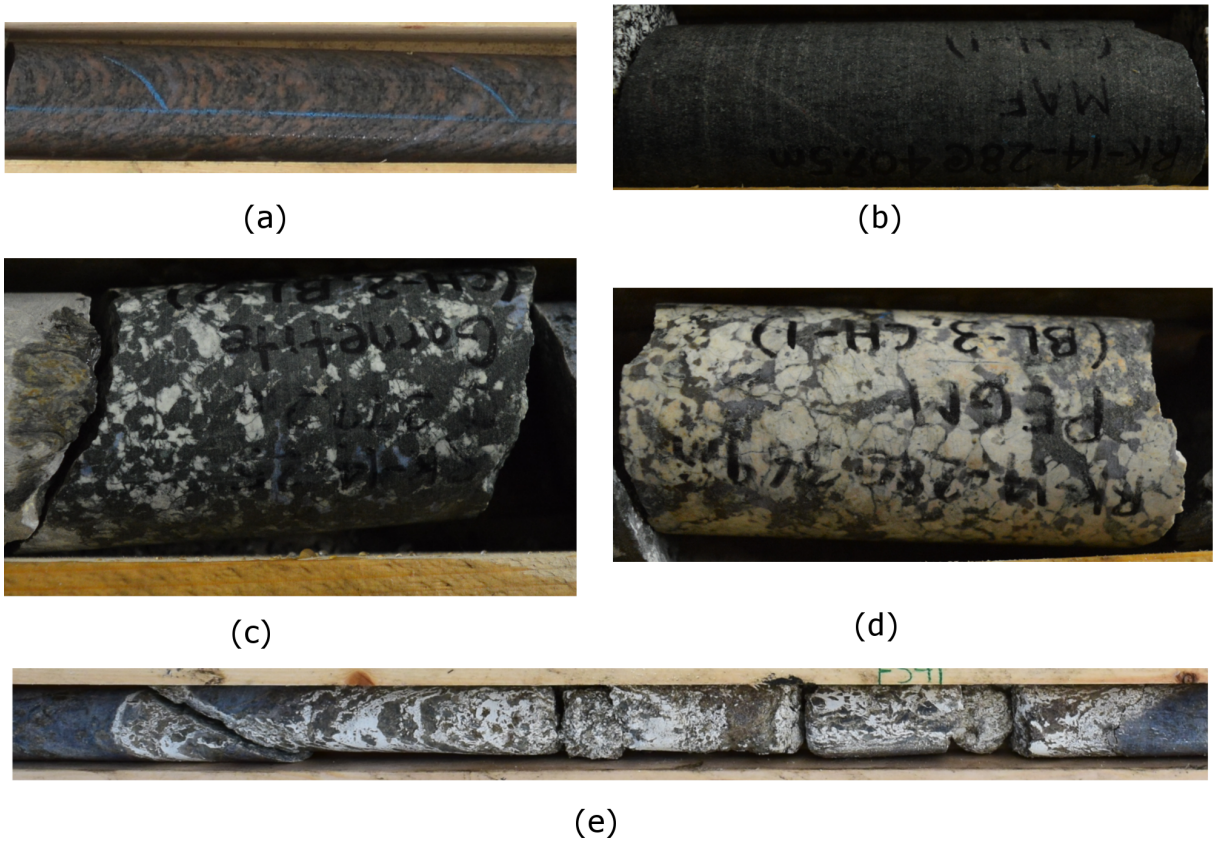

Figure 11: a) Granodioritic gneiss. b) Gabbro. c) Garnetite. d) Pegmatite. e) Dravite breccia.

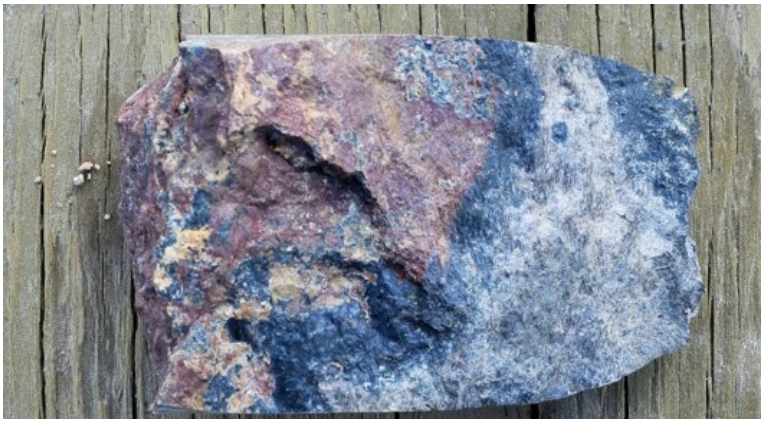

Figure 12: Well developed redox front with uraninite (From Nexgen presentation, 2014)

Hematite alteration is mostly found close to the unconformity , possibly representing remnants of the oxidized paleoweathering profile, and in the sandstone. It is also directly associated with the mineralization where it may represent one of the latest alteration stages. Retrograde alteration is thought to be related to late faulting, typified generally by variable degrees of chloritization of mafic minerals and clay alteration of feldspar (mainly illite, sericite and dravite). Extreme alteration (illite, hematite and chlorite) is mainly restricted to 1-3 m haloes near the uranium hosting minerals. Dravite alteration (minerals of the tourmaline group were shown to be magnesiofoitite in other areas of the Athabasca basin; Zhang et al., 2001; Rosenberg and Foit, 2006) is usually associated with bleached zones found within 10 meters of mineralization. Dravite is commonly observed near mineralization but forms as late veins and breccias that crosscut all pre-existing minerals. Sulphide mineralization at Arrow consists mainly of pyrite often associated with milky quartz veins and carbonate, it is found crosscutting the main foliation as well as late alteration phases.

The Arrow deposit is composed of a series of moderately or steeply inclined tabular veins and lenses associated with reverse faults characterized by mylonites and shears; these faults often develop in the less competent graphitic metasedimentary rocks. Major graphitic structures usually are parallel to the foliation whereas dravite-rich structures are at angles suggesting a later paragenesis (Hillacre, 2015; Mathisen and Ross, 2016). Uranium mineralization often occur in association with these structures but sometimes has been observed in faults cross-cutting non-graphitic rocks. Uranium mineralization at the Arrow deposit is predominantly in the form of uraninite, with less amounts of coffinite and uranophane, and is apparently structurally controlled. The Arrow deposit shares many similarities with the Eagle Point deposit in the north-eastern Athabasca basin, which is also a basement-hosted and structure-controlled uranium deposit (NexGen presentation, 2015; Ainsworth, 2016).

The ages obtained for initial uranium mineralization in unconformity related deposits in the Athabasca Basin are typically 1.4-1.6 Ma, although significantly younger ages have

Figure 13: Quartz and hematite breccia from the paleoweathering profile hosted in hematite altered psammo-pelitic gneiss

Figure 14: Milky white quartz vein hosted in gabbro

also been measured which are interpreted to represent partial to total resetting of the uraninite system due to fluid circulation (e.g. Cumming and Kristic, 1992; Alexandre et al., 2009). Given the alteration affecting the mineralized shear zones, and the complex relationships between quartz events examined in this study, there have likely been multiple re-mobilization and/or U-alteration events after the main mineralization phase at Arrow as well.

Quartz events at Arrow Quartz-rich veins, breccias and cavities are well developed in the basement at the Arrow deposit, have complex cross-cutting relationships, and exhibit diverse colorations. Four types of quartz in veins, breccias and cavities can be dinguished on the basis of coloration:

- Translucent to milky quartz. (Figure 19,21)
- Milky quartz often associated with hydrothermal breccias. (Figure 13,14,22)
- Pink quartz usually in veins or breccias, associated with dravite. (Figure 17,23,20)
- Grey smoky quartz in veins and cavities. (Figure 15,16)

Graphitic psammipelites are the main host lithologies in the basement at the Arrow deposit and are characterized by quartz grains of “bluish” tint (hereafter referred to as blue quartz).

Figure 15: Dark gray smoky drusy quartz near mineralization within mineralized graphitic shear zone

Figure 16: Smoky quartz crystals

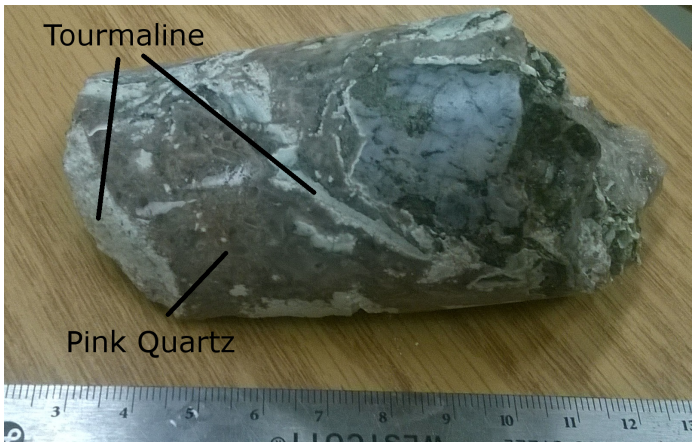

Figure 17: Pink quartz and dravite breccia hosted in psammo-pelitic gneiss

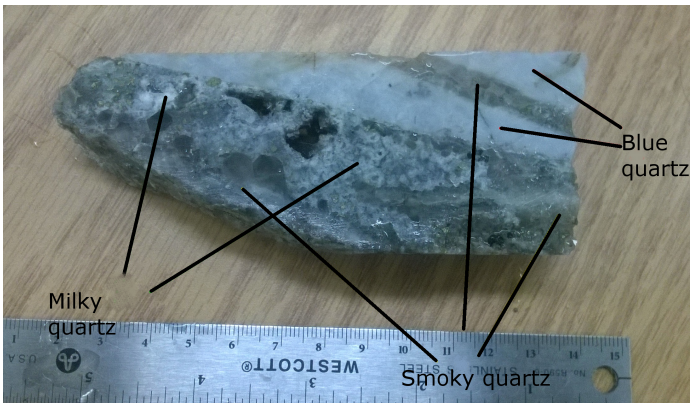

Figure 18: Milky (latest) and smoky (earlier) quartz events hosted in silicified basement rock (blue quartz, earliest).

Figure 19: Translucent drusy quartz crustals withing fracture in psammo-pelitic gneiss

Figure 20: Pink quartz vein lined with dravite withing psammo-pelitic gneiss

Figure 21: Transparent drusy quartz stained with hematite hosted in psammo-pelitic gneiss

Figure 22: Milky white quartz vein hosted in psammo-pelitic geniss

Figure 23: Pink quartz breccia with radioactive clasts within graphitic shear zone

5 Sampling protocols and analytical methods

5.1 Sampling protocols

Collection of the samples placed emphasis on obtaining a representative selection of each different quartz event identified as well as an even spacial distribution. A total of 271 samples (93 sandstones and 178 basement rocks, of which 97 have "drusy" quartz in veins, breccia and cavities) were collected from the Arrow property and its surrounding areas.

Sandstone samples from the Manitou Falls formation were collected from each drill hole available at Arrow (up to AR-16-75), taken preferably 1 m above the unconformity. Additional sandstone samples were collected from regional exploration holes, including two other discoveries (i.e., Bow and Cannon). Vertical sampling of the sandstones was not done, because only ∼10-40 m of sandstones are present at Arrow. In the sandstone unit numerous different layers were observed with variations in grain size and coloration. To obtain representative values for the sandstone in that location, the sample was taken from the uniform layer that was most common in the 4 meter interval above the unconformity.

Of the 271 samples, 184 (90 sandstones and 94 basement rocks) were selected for the separation of quartz for EPR analyses.

Sandstone samples were first soaked in water for a day, lightly crushed into smaller pieces, and then washed in an ultrasonic bath. The resulting grains were sieved (500 μm in diameter) and dried in air. Pure quartz grains were then handpicked under a binocular microscope. For the basement rocks, 7 representative psammopelites were selected and contain quartz grains of a "blueish" tint. Other basement rocks selected contain quartz-rich veins, breccia and cavities, which are grouped according to the color of quartz (24 pink, 16 smoky, 24 milky, and 23 translucent) and were thought to represent different generations of quartz crystallization. Several basement samples contain multiple generations of quartz (i.e., cross-cutting veins), which were separated and analyzed independently. The quartz-rich veins, breccia and cavities in basement rocks were carefully cut from their hosts and were lightly crushed and washed in an ultrasonic bath, where necessary. Quartz grains were again obtained by handpicking under a binocular microscope. Finally, all samples of quartz separated were grinded into a fine powder (¡100 μm in diameter) using an agate ring mill.

Two quartz separates from a sandstone (2502096) and a quartz-rich breccia from a basement rock (0801635), which have the highest intensities of hole-like defects, were selected for annealing and neutron irradiation experiments. These quartz separates were first annealed at 500°C for 24 hour and then subjected to neutron irradiation (i.e., a flux of 10^{12} n/cm^2 for 3 hours) in the Slowpoke-2 reactor at the Saskatchewan Research Council.

Table 3: **Number of samples analyzed for different lithologies and areas**

	Basement	Arrow Sandstone	Rook I Sandstone
Number of Samples	94	47	43

5.2 EPR spectroscopy

All powder and selected single-crystal samples of quartz, include the two after neutron irradiation, were analyzed at room temperature on the Bruker EMX spectrometer at the Saskatchewan Structural Sciences Center. Experimental parameters for EPR analyses were those optimized in previous studies (Botis et al., 2006; Hu et al., 2008; Pan et al., 2013): microwave frequencies of ≈9.87 GHz, a modulation frequency of 100 kHz, a modulation amplitude of 0.08 mT, microwave powers of 0.2 mW and 6.35 mW, and a spectral resolution of 0.015 mT (1024 points over 15 mT) . The powder EPR spectra of all samples were measured on approximately the same amount of powder (100±1 mg) to facilitate direct comparison. Also included in powder EPR analyses are previously investigated samples (5 drusy quartz samples from the sandstone above the McArthur River deposit of which: 2 from the alteration halo and 3 from less altered units; and 5 detrital quartz samples from sandstones in the Maw Zone).

5.3 CL imaging and spectroscopy

Polished thin sections of 20 quartz separates from the basement (11 smoky, 3 pink, 5 translucent, 1 milky; all drusy quartz) were prepared for microscopic and cathodoluminescence investigations. CL microscopy and spectroscopy were performed on carbon-coated thin sections using a hot-cathode CL microscope HC1-LM (Neuser et al., 1995). The system was operated at 14 kV and 0.2 mA (current density ∼10 μA/mm^2) with a defocused electron beam. Luminescence images were captured "on-line" during CL operations using a peltier cooled digital video-camera (OLYMPUS DP72). CL spectra in the wavelength range 370 to 920 nm were recorded with an Acton Research SP-2356 digital triple-grating spectrograph with a Princeton Spec-10 CCD detector that was attached to the CL microscope by a silica-glass fiber guide. CL spectra were measured under standardized conditions (wavelength calibration by a Hg-halogen lamp, spot width 30 μm, measuring time 5 s). Irradiation experiments were performed to document the behaviour of the quartz samples under electron irradiation. Samples were irradiated 10 minutes

under constant conditions (14 kV, 0.2 mA) and spectra were measured initially and after every 1 minute.

6 Results and Discussion

6.1 Powdered EPR spectra

Three main spectral types where identified in the quartz samples collected at Arrow (Figure 24):

- Sandstone detrital quartz
- Spectra of selected smoky quartz
- Basement drusy quartz

The spectra from Arrow are compared to a reference spectrum of drusy quartz from the alteration halo above the McArthur River deposit. Figure 24 shows that the representative Arrow spectra are similar to those of their counterpart from the Athabasca basin. Both identify the presence of the well known E_1' center and a suite of hole like centers, including H_1', H_2', H_3', H_4', H_7' (Botis et al., 2005; Botis et al., 2006; Pan et al., 2006; Botis et al., 2008; Hu et al., 2008; Pan et al., 2008; Nilges et al., 2009; Pan et al., 2013).

The hole-like centers share similar g-intermediate (g_{int} ~2.007) and g-minimum (g_{min} ~2.003) values but can be identified by their unique g-maximum (g_{max} ; shown in Figure 24) values and diagnostic peak shapes (Nilges et al., 2008).

For example The ozonide radical O_3^- and the superozide radical center O_2^- (respectively H_7' and H_1') are resolved as narrow peaks at g_{max} values of 2.030 (Mashkovtsev et al., 1978) and 2.017 (Botis et al., 2008) both of which have very small ^{27}Al superhyperfine structure. The series of broad peaks centered at g_{max} values of ~2.035 and ~2.030 are part of centers H_2' and H_4' (respectively B/B'(Pan et al., 2008) and G/G'), that are characterized by significant ^{27}Al superhyperfine structures (Nilges et al., 2008; Pan et al., 2008; Nilges et al., 2009; Pan et al., 2009).

One salient feature in Figure 24 is that the hole-like centers vary widely between different quartz samples. For example, the superoxide radicals H_4' with broad peaks arising from considerable ^{27}Al superhyperfine structures are abundant in most samples but are absent in others, resulting in significantly different EPR spectra . Detrital quartz in the Athabasca sandstones is also characterized by the presence of the peroxy radicals H_3' (i.e., D/E at g_max ~2.05; Pan et al., 2009), which are conspicuously absent in quartz from the basement. These centers were also observed in regional exploration holes at Bow, Cannon and Harpoon discoveries in the same property.

EPR analyses of two selected samples that were first thermally annealed and then reactivated by neutron irradiation show that the peak at g_{max} ~2.05 is re-stored in detrital

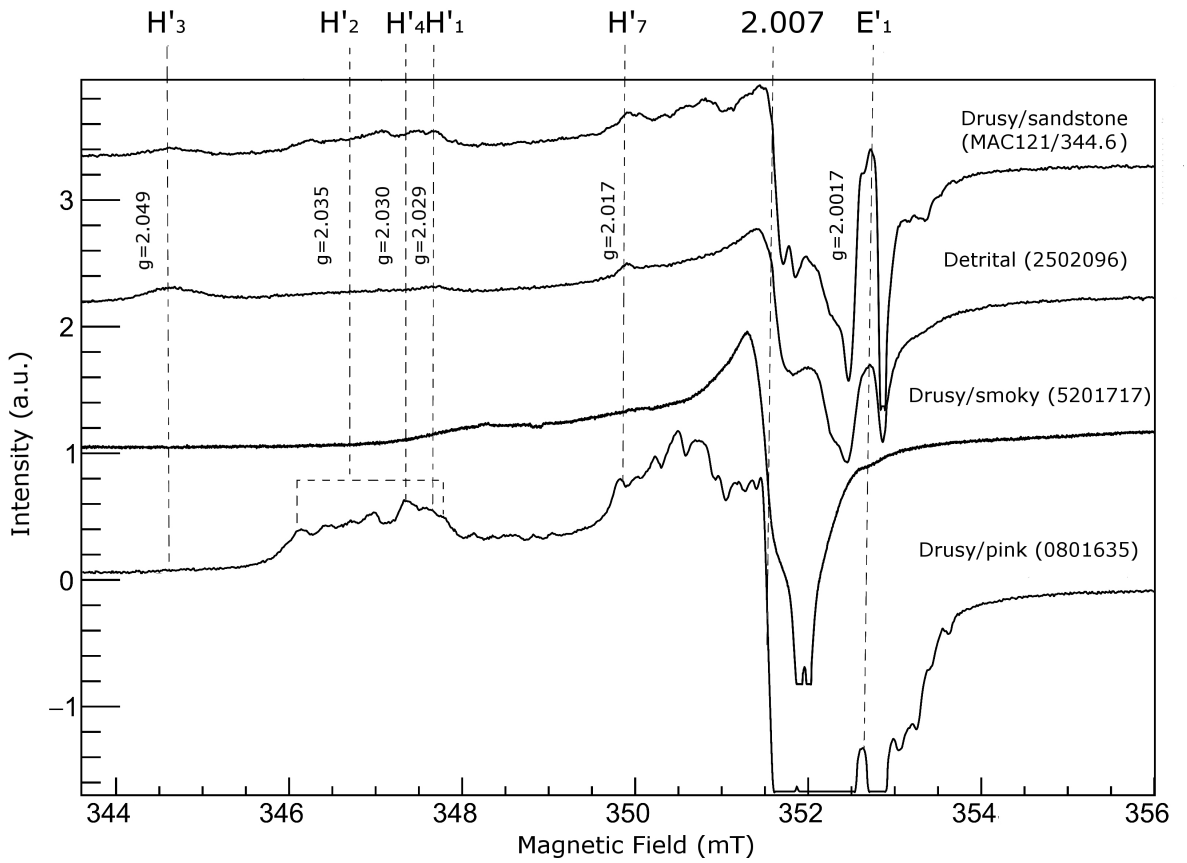

Figure 24: . Representative powder EPR spectra of quartz from the Arrow deposit (measured at microwave frequencies of ∼9.87 GHz and microwave power of 6.35 mW). Also shown for comparison is that of a drusy quartz from the McArthur River deposit (MAC121/344.6 ; Hu et al., 2008). The hole centers are marked by their characteristic g_{max} peaks.

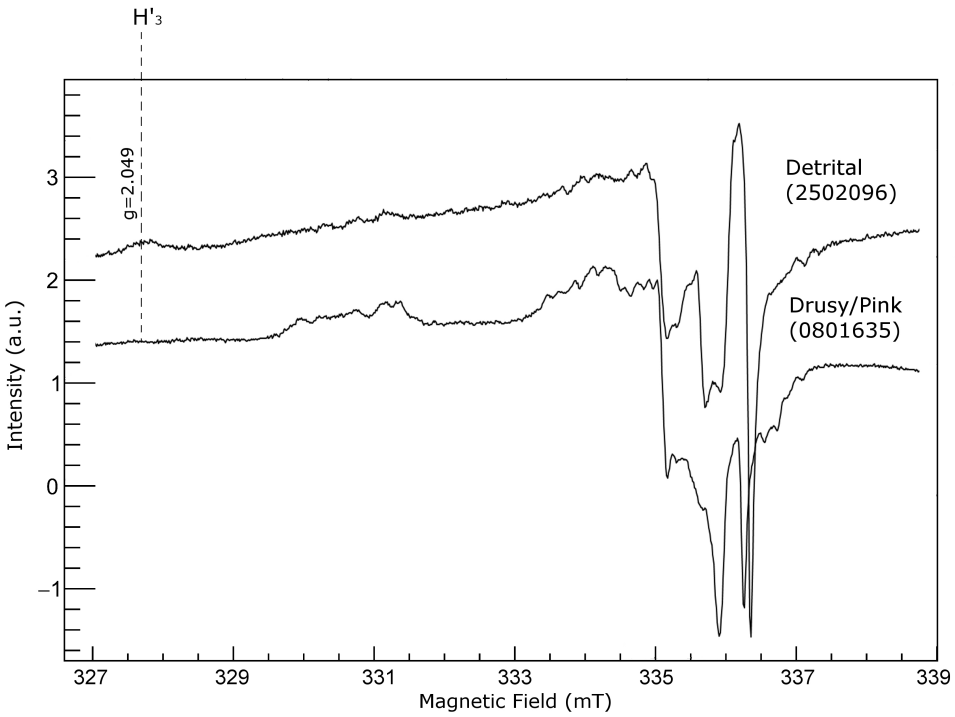

Figure 25: Comparison of neutron irradiated spectra of detrital quartz sample 2502096 and pink quartz 0801635. Center H_3' is marked.

quartz, but remains absent in the hydrothermal quartz from the basement (Figure 25). The contrasting behviour of the peroxy radicals H_3' in the two selected quartz samples suggests that the hole-like centers are most likely linked to their diamagnetic precusors, which in turn may be related to growth defects formed during the crystallization of quartz.

Another parameter that differentiates the spectra is the relative intensity of the defects; while sandstone samples from other areas in the basin do present the previously mentioned H_3' centers (Hu et al., 2008; Pan et al., 2013) their intensity relative to the H_7' center (that is used as the reference peak to calculate the ratio in table 4) appears to have regional variations.

As can be seen from the table the ratio between centers H_3' and H_7' is similar between Arrow and surrounding discoveries but differs by an order of magnitude from the reference spectra (reference samples used in the comparison are drusy quartz from the sandstone units above McArthur River deposit). Furthermore ratios between other defects and H_7' seem to remain constant (within the variance) within all samples including reference ones. This variation may again be related to both precursor defects and irradiation processes and requires further comparison with quartz from different locations in the Athabasca basin.

To summarize, spectral differences appear to be of 2 kinds: lithological (e.g. presence or absence of H_3' centers) and regional (variation in relative intensity of H_3' centers). It would be of interest to investigate if other areas of the basin exhibit similar differences

Table 4: **Ratios between hole centers for different samples**

	C'/#1	C'/G	C'/D+E
Basement	1.41 ± 0.10	1.54 ± 0.27	n/a
Arrow	1.34 ± 0.43	1.69 ± 0.31	0.92 ± 0.19
Bow	2.27 ±1.1	1.50 ± 0.41	0.99 ± 0.23
Cannon	1.44 ± 0.31	1.60 ± 0.55	1.28 ± 0.62
Regional	n/a	n/a	0.80 ± 0.3030
Reference	1.54 ± 0.20	1.82 ± 0.39	12.6 ± 8.4

between detrital sandstone and drusy basement quartz and if other defects are affected by lithology.

Figure 26 shows that there is a general positive correlation in the two types of radiation-induced defects in quartz at Arrow. This correlation suggests that alpha particles are the dominant source of radiation, whereas other types of radiation (e.g., γ rays associated with potassic alteration) are relatively minor at Arrow. Therefore, the electron-like centers, which are readily detected and quantified than their hole-like counterparts, in quartz are also useful vectors for evaluating uranium-bearing fluids .

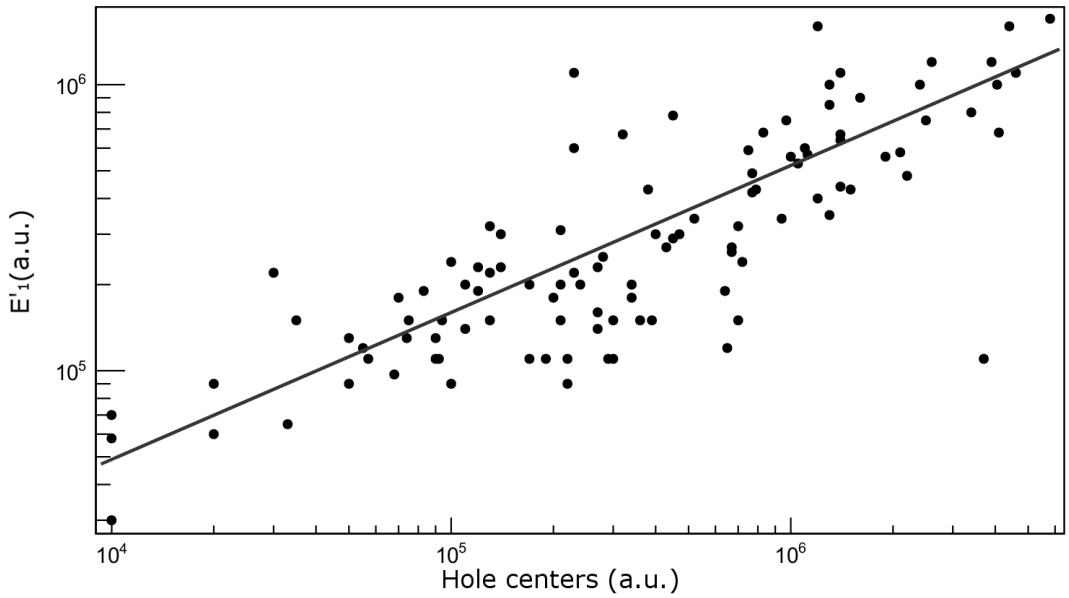

Figure 26: Correlation in the EPR intensities between the E'1 center and the hole centers in quartz at the Arrow deposit. The calculated correlation coefficient (R2) is 0.667.

6.2 Defect intensity distribution

6.2.1 Basement

As previously mentioned drusy quartz in the basement was divided into pink, milky, translucent and smoky. Additionally blue quartz grains were present within the psammo-pelites of the crystalline basement. All mentioned quartz types were analyzed for RIDs to evaluate their association with U-related events. Given that alpha radiation gives rise to a whole host of different defects with different g-values, the peak at g≈2.007 was taken as a gross estimate of the amount of hole like centers due to the overlapping of g-intermediate principal values in its vicinity. Since the collected spectra is the first derivative of the absorption it was baseline corrected and then integrated to obtain a better estimate of the total concentration of α-related defects.

To contextualize and provide a frame of reference for the intensities of the analyzed samples they were compared with 5 reference samples from McArthur River, 5 from the Maw Zone and with samples of known intense irradiation (e.g. covered in radioactive clay, in contact with uraninite clasts).

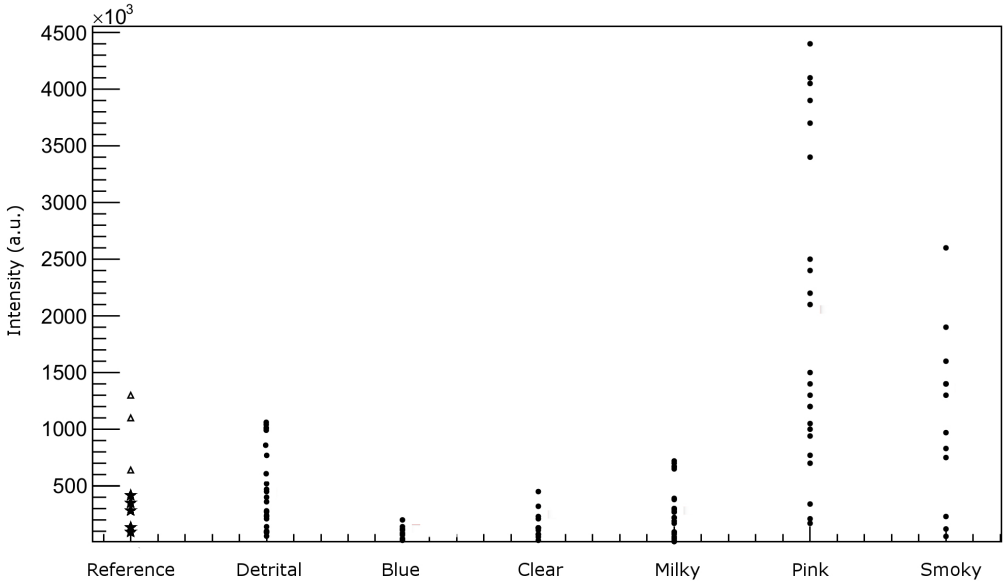

Figure 27: Summary of the EPR intensities of the hole centers (as approximated the g_{int} = ∼2.007 peak height) in different types of quartz at the Arrow deposit and surrounding areas. Also shown for comparison are those of three samples of drusy quartz in less altered sandstones at the McArthur River deposit (marked with triangles; Hu et al., 2008) and five samples of detrital sandstone from the Maw Zone (marked with stars; Pan et al., 2013). Two samples of drusy quartz in alteration haloes at the McArthur River deposit contain higher intensities (∼$5.8{\cdot}10^6$ and ∼$6.4{\cdot}10^6$) and are not shown.

Blue quartz from basement psammo-pelite was found to contain the lowest amounts of radiation damage mostly with no visible silicon vacancy centers. This confirms that U-

fluids did not permeate through the basement metamorphic rock but rather were strictly structurally controlled as suggested by the deposit conformation. EPR spectra show that both translucent and milky quartz in veins and cavities have slightly higher radiation-induced defects than the blue quartz in the host rocks. Pink quartz exhibited the highest concentrations of RIDs than any other event, it was also observed out of all the pink quartz samples the ones that presented a smoky tinge were on average more damaged. Goreva et al. (2001) showed that pink nanofiberous inclusions of dumorterite are present in rose quartz from 29 different pegmatite and massive vein localities worldwide and are the cause of coloration. The smokiness arises instead from the $[ALO_4]^0$ centers which require low-temperature EPR measurements for detection and are not investigated in this study (Nuttall and Weil, 1981). Smoky quartz also presents a high number of defects and is comparable to the pink event.

It is of note that the RID concentrations, even in samples that were more exposed to radiation (adjacent to mineralization, in contact with radioactive clay, ...), are lower than reference drusy quartz sandstone from the alteration halo of the McArthur River deposit. In regards to this it must be considered that the data obtained measures just the amount of exposure, per surface area of contact, that a sample has experienced. There are a multitude of factors that need to be considered when making comparisons between individual samples or different lithologies.

- Surface area: assuming the crystal is already formed when the U-fluids come in contact with it sandstone grains will have a greater exposure area relative to total silica mass as compared to structures in the basement.

- Timing: crystals that are exposed to U continuously during their growth period would present a much higher defect density than those exposed afterwards. This is due to the low penetration power of α particles (40-50nm).

- Duration: the longer the crystal is exposed to radiation the more defects it will present , up to saturation.

- Fluid speed: this directly correlates with time as the faster the U-fluids are flowing the less time they will be in contact with the quartz (assuming constant U amounts). Fluid speed will be different in different sandstone units (based on grain size and cohesion) and in the basement where it will flow at a faster rate through the fractures and shears.

- Concentration: the amount of U in the fluids will for obvious reasons influence the amount of radiation emitted.

- Temperature: defect concentrations were shown to vary after thermal treatement resulting in an increase or decrease according to temperature and specific defect.

Based on all these factors one explanation for the (relatively) low amount of defects in irradiated basement quartz would be the higher speeds of the fluids and the lower area of exposure of the quartz grains. Other of the listed factors might contribute to the observed RID concentrations but it is not possible to quantify them .

To complement the study of defect concentration in relation to quartz type its distribution relative to U mineralization was also studied. Distance from mineralization was calculated from the sample collection location to depth of closest measured radioactivity from the core exceeding 1000 cps along the hole. The observed distribution (Figure 28) seems to follow an exponential trend, increasing the more it nears actively radioactive areas. This illustrates that most of the highly irradiated samples are within 20 meters downhole of U minerals. Assuming that mineralization is distributed in approximately vertical lenses and average drill hole dip= 70° , the actual range would be $\sim$ 7m. This is in comparison to unconformity based deposits where radiation damaged samples can be found at more than a hundred meters distance from the deposit (Botis et al., 2006).

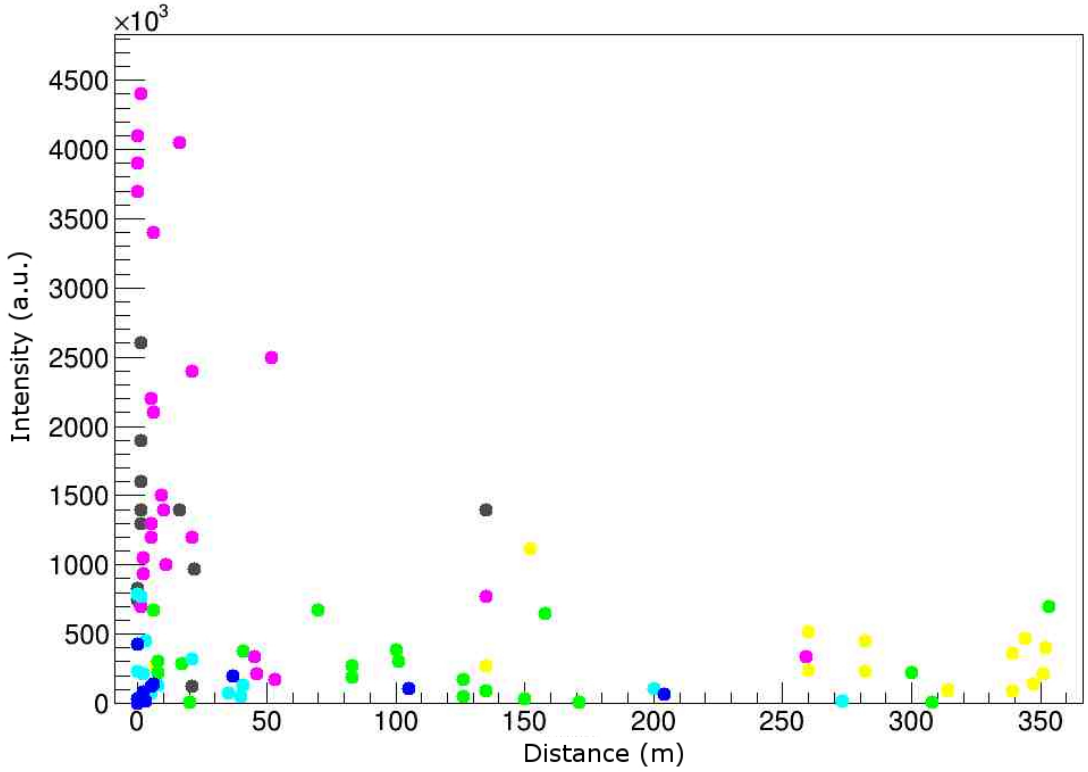

Figure 28: RIDs concentrations relative to downhole radioactivity. Blue=blue quartz, Cyan=clear quartz, Green=milky quartz, Pink=pink quartz, Grey=smoky quartz, Yellow=detrital sandstone quartz.

It is significant that quartz with low RIDs is distributed at all depths regardless of proximity to mineralization, samples up to 0.1m from high radioactivity areas were barren of defects. This is due to the low penetration power of α particles $\sim$ 30-40nm. On

the other hand, quartz with high defects appears to only occur nearby U-mineralization. Since the vast majority of quartz samples investigated in this study do not contain detectable uranium-rich minerals (apart from two, a breccia with radioactive clasts and drusy crystals in cavities containing coffinite), the observed radiation-induced defects in quartz must record the uranium-bearing fluids.

Considering the spatial limitations of radiation damaged quartz and the absence of RIDs from the quartz grains of the psammo-pelite, it can be inferred that the U-bearing fluids responsible for the Arrow deposit were concentrated in fractures and shears and didn't permeate through the crystalline basement. Previous studies in the eastern part of the basin noted that quartz veins significantly below mineralization are almost EPR inactive, this was interpreted to support the conclusion of Fayek and Kyser (1997) that the basement fluids were deficient in uranium. The present results show that drusy quartz in the basement at the Arrow deposit is far more complicated and significantly different from those observed in the eastern Athabasca basin suggesting that a different approach, more focused on structures, is necessary when studying basement hosted deposits.

6.2.2 Sandstone

The EPR intensities of detrital quartz grains from sandstone samples at Arrow are on average an order of magnitude lower than their counterpart in alterations haloes at the McArthur river deposit (these reference samples are shown in green in Figure 27, samples from altered areas are not shown for clarity purposes; Hu et al., 2008; Botis et al., 2006). The intensities are only comparable to samples far from mineralization and outside the alteration haloes and with the U-poor system of the Maw Zone suggesting that the Arrow sandstones were not subjected to the flow of U-rich fluids. For this study the baseline concentration of defects of regional sandstones was calculated by averaging the values obtained from exploration holes outside of Arrow that didn't intersect mineralized systems and was found to be $\sim 200000 \pm 70000$ a.u.

The intensity of RIDs in regards to spatial distribution was then simulated by interpolating the concentrations obtained from the drill holes at Arrow with the calculated baseline. By plotting the intensity of the defects in sandstone samples on a map of the deposit it is possible to observe the relationship between concentration and mineralization zones. Figure 29 shows that EPR intensities in detrital quartz are highest in north east part of the deposit and decline to the southwest and perpendicular to the strike of the deposit .

The U-bearing fluids can have basement or basinal origin: if the fluids were from the basin a high amount of defects would be observed along the pathway that they followed towards Arrow. No such high-defect corridor is observed and defects values decline to background levels towards the edges of Arrow further confirming that basinal fluids were lacking in U. Instead high EPR areas are clearly restricted to sandstones above mineralized basement zones. Because of the interpretation that the basinal fluids are not rich in U it can be assumed that the fluids that created the observed defects were of basement origin. In this model the structurally controlled fluids would in part overflow (based on the distance and the amounts of structures between basement mineralization zones and the unconformity) into the basin creating the measured defects.

Due to the vertical nature of the major basement structures this model would predicts higher RID concentration in sandstone rocks above near-unconformity mineralization lenses where more U-rich fluid leaves the basement. This is consistent with the pattern shown in Figure 30 as intensity rises to the N-E ,where high radioactivity zones have been identified near the unconformity, and falls to the S-W where the deposit slightly dips (NexGen presentation, 2016).

Additionally the sandstone above the intrusive package that lacks major structures is characteristically absent in radiation-induced defects and records some of the lowest values measured. (Figure 31).

Holes connected to nearby discoveries were also studied (Bow, Cannon) and it was

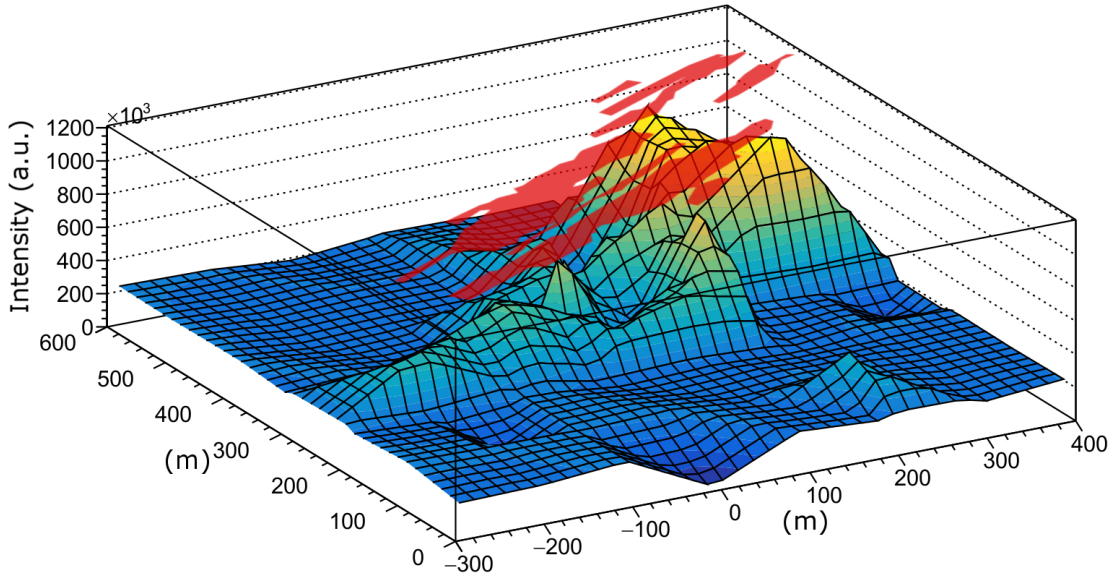

Figure 29: 3D representation of defects intensity in regards to their spatial distribution. Above is positioned a plan map with highlighted areas of U-mineralization. Spatial coordinates are relative to an arbitrary origin and are in meters.

found that they also exhibited abnormally high RIDs concentrations (relative to the base in the area) in a selected number of holes. Unfortunately the small number of diamond drill holes in these areas makes it impossible to obtain detailed spatial distribution similar to the one obtained for Arrow. A limited number of samples from the Bow discovery (Figure 32) exhibited defect concentrations comparable to reference values from altered halo at McArthur River deposit, this could indicate multiple refluxes of U-bearing fluids out of the basement that would accumulate more defects than in other areas. Higher U concentrations would be improbable since the discovery there is significantly smaller than at Arrow. Regional holes outside Bow and Cannon produce spectra deficient in silicon vacancy centers in all cases apart from samples RK85096, RK84097 and RK72126.

These results from detrital quartz along the unconformity supports the use of EPR as a promising tool for studying the loci of U-bearing fluids in the Athabasca basin (Pan et al., 2013) as well as in the exploration of basement hosted mineralization.

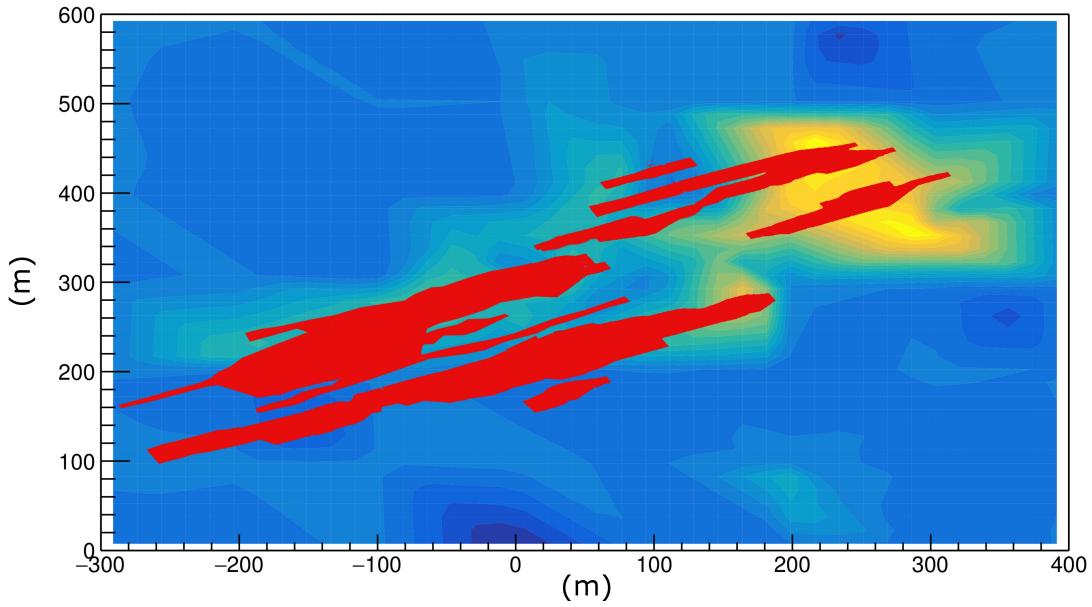

Figure 30: Contour plot of defects intensity in regards to their spatial distribution. Overlaid is an outline of the main mineralization areas of Arrow. Spatial coordinates are relative to an arbitrary origin and are in meters.

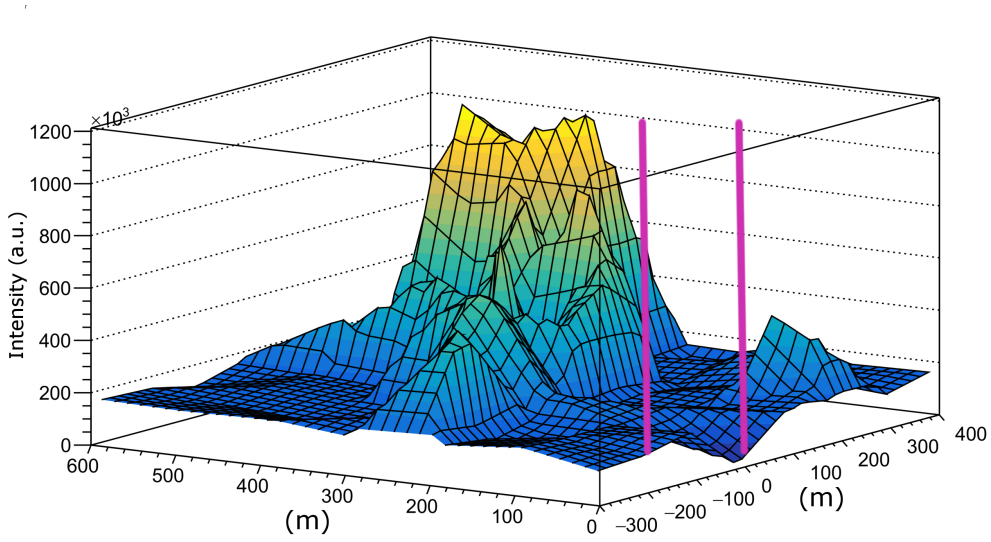

Figure 31: Contour plot of defects intensity in regards to their spatial distribution (as in Figure 29). View is from the S-W. Highlighted in purple is the area above the intrusive unit.

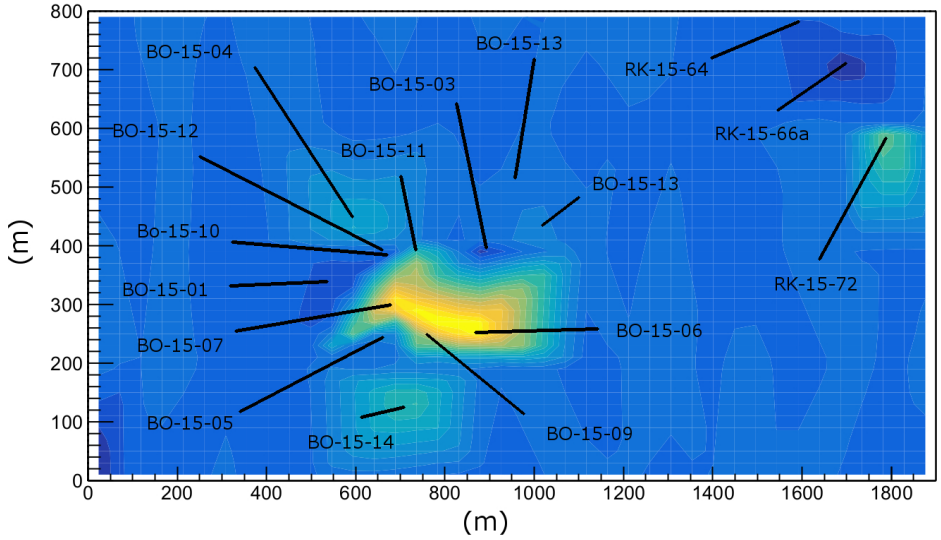

Figure 32: Contour plot of defects intensity in regards to their spatial distribution. Shown is the Bow discovery (holes labelled BO) and regional holes to the north-east. Spatial coordinates are relative to an arbitrary origin and are in meters.

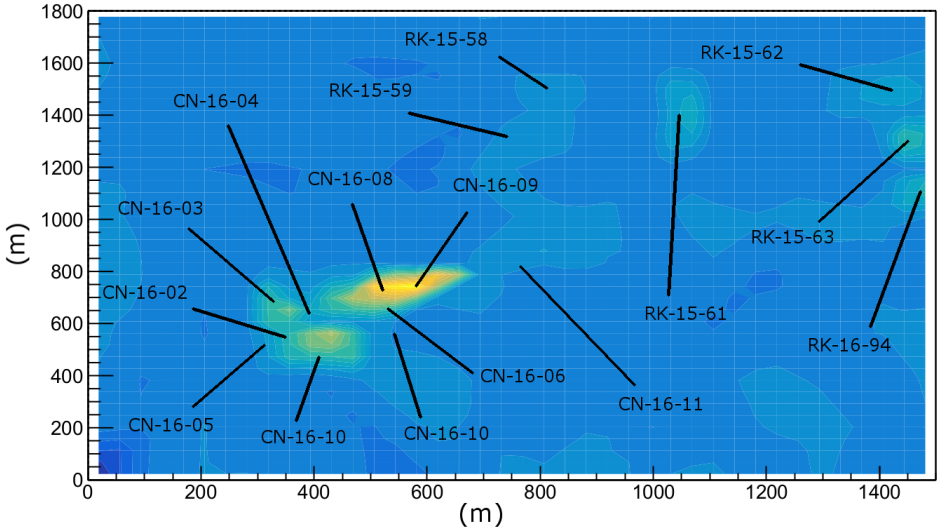

Figure 33: Contour plot of defects intensity in regards to their spatial distribution. Shown are the Cannon discovery (holes labelled CN) and regional holes between it and Bow. Spatial coordinates are relative to an arbitrary origin and are in meters.

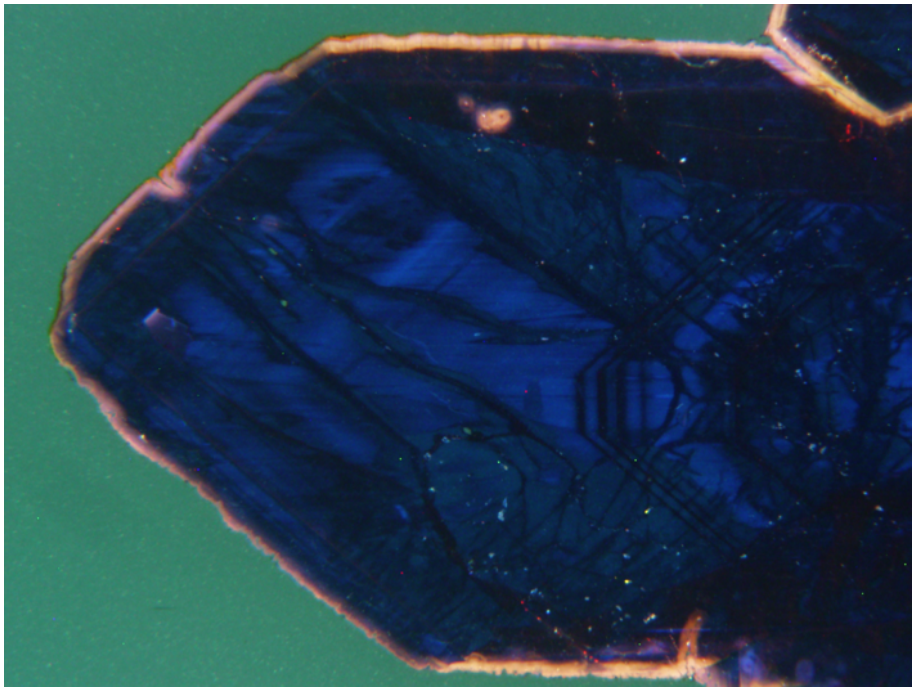

Figure 34: CL image of sample 2801247. Radiation damage rims in yellow-orange can be seen in the outmost layer of the crystal.

6.3 Cathodoluminescence analysis

Selected samples were also subjected to cathodoluminescence spectroscopy and microscopy. Blue quartz in semi-pelites from the basement at Arrow are characterized by a bulk CL of blue color with a broad peak centered at ∼450 nm. The 450nm emission is due to the recombination of the self-trapped exciton (STE). The self-trapped exciton involves an irradiation-induced electron hole pair (Frenkel pair consisting of an oxygen vacancy and a peroxy linkage). This 450 nm emission is the most common CL emission in amorphous and crystalline SiO_2 and more or less present in all quartz types. The 500 nm emission can be related to the substitutional impurity centers in the quartz structure. All samples analyzed featured a bulk of blue CL color with broad peaks centered around mentioned values.

Transluecent and milky quartz crystals do not have alpha-particles-induced CL halos, patches or continuous rims. Smoky quartz, on the other hand, is characterized by the common presence of yellow-orange, continuous rims with a width of ∼30-50 μm (Figure 34), which have a broad peak centered at ∼650 nm in CL spectra (Figure 35d) and are readily attributed to alpha-particles-induced damage (Botis et al., 2005). In particular, the continuous rims in smoky quartz often cross-cut the outermost growth zoning (Figure 35c). In addition, characteristic CL haloes and patches around uranium-bearing minerals are also common in smoky quartz (Figure 35a). Contrary to smoky samples, alpha-particles-induced CL halos, patches or continuous rims are conspicuously absent in pink

quartz, including those from the two samples with the highest radiation-inducded defects as detected by EPR. In some samples slight zoning in radiation rims can be observed (Figure 35b): orange, violet, bluish) that can be attributed to decreased lattice damage due to the range of the α radiation.

CL data for the most part confirms EPR results with milky and clear quartz types characterized by low EPR signals have no CL rims while high intensity smoky quartz shows distinct radiation-related CL. Rims in smoky quartz are consistent with post-growth irradiation as shown by rim width and the cross-cutting of growth zoning (Figure 35c). The pink quartz is particularly interesting for its elevated radiation-induced defects in EPR spectra (Figure 27) but a general absence of alpha-particles-induced CL halos, patches or continuous rims. Similar features have been observed previously in drusy quartz from sandstones at the McArthur River deposit, for which partial HF dissolution experiments demonstrated that radiation-induced defects are distributed homogeneously in such crystals (Hu et al., 2008). It was interpreted that such drusy quartz crystallized from uranium-bearing fluids (defects formed during crystal growth) and was not overprinted by late uranium-bearing fluids.

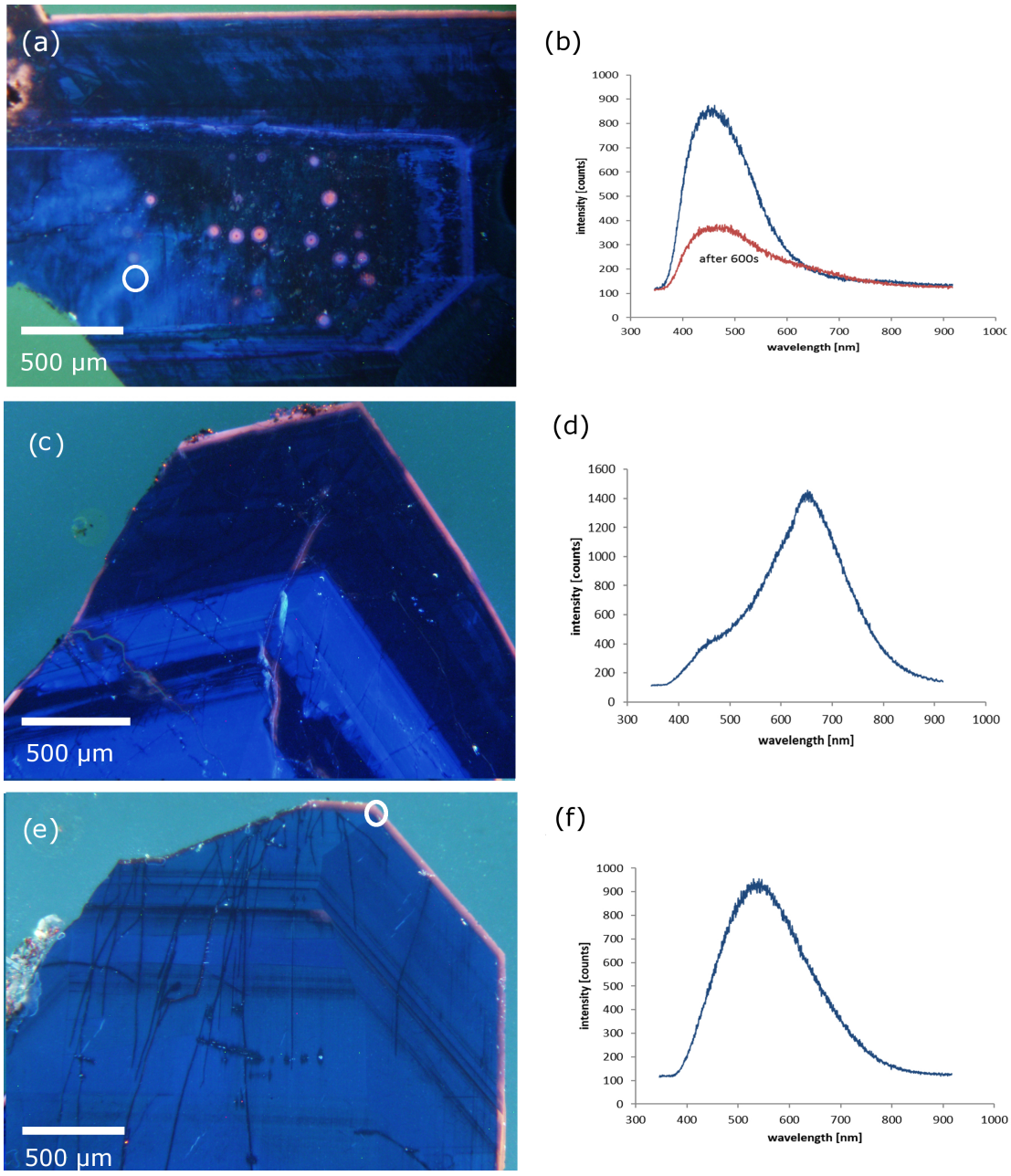

Figure 35: Representative CL images (a,c,e) and CL spectra (b,d,f) of drusy quartz from the basement at the Arrow deposit: a) halos around coffinite inclusions in smoky quartz;(4831698) b) ∼450 nm peak from blue CL color in a); c) CL rims overprinting quartz zoning (5711425); d) CL spectrum of smoky quartz sample (2801247) showing characteristic peak at ∼650 nm. e) continuous rim crosscutting the growth zoning in smoky quartz (4831698); f)CL spectra showing the broad peak centered at ∼650 nm superimposed with the blue CL signal at ∼450 nm.

6.4 Paragenesis

Based on the CL data and the RID distribution the different quartz events were associated with the relative phase.

Milky and clear quartz have no association with mineralization phases because of the lack of both EPR detected defects and CL rims or haloes around inclusions. Consequently these quartz types are thought to be the latest since if growth had occurred prior or during one of the U events CL rims would be present overprinting the outmost crystal layers.

Pink quartz samples were found to exhibit on average the highest amounts of defects. From CL imaging it was identified that the irradiation occurred during the crystal growth. It seems likely then that the growth of this quartz type coincided with the main mineralization phase where the U-bearing fluids created a significant amount of defects within the quartz. This suggestion is supported by the common association of pink quartz with dravite alteration (i.e., magnesiofoitite and dravite; Zhang et al., 2001; Rosenberg and Foit, 2006), which are known to occur in close spatial and temporal association with uranium mineralization in the eastern Athabasca basin. Smoky quartz instead exhibited radiation damage rims along the outer edges of the crystals and cross-cutting growth zoning signifying bombardment post-growth. This is most in agreement with later phases of U remobilization. Quartz growth in basement structures in-between these events would be afterwards subjected to radiation bombardment creating the presently observable CL rims.

Table 5: **Regional paragenesis and associated quartz events**

Regional metamorphism	• Metamorphic assemblages • formation of graphite	• Blue
Retrograde metamorphism	• Quartz-chlorite alteration and veins	• Clear • Milky
Paleoweathering	• Paleoweathering profile development	• Milky
Uranium mineralization related events	• Massive sericite alteration • Secondary chlorite alteration, quartz veins • Main stage U-rich fluids: uraninite + hematite, calcite, chlorite, sudoite	• Pink
U alteration and other phases	• Alteration and recrystallization of uraninite • Coffinite formation • Hematite alteration • Early dravite	• Smoky
Latest veins and alteration	• Chlorite alteration • Calcite, quartz veins, sulphides • Late dravite veins	• Clear • Milky

7 Conclusions

The principal results of this EPR study of quartz at the Arrow deposit are as follows:

- From EPR spectra a host of different hole centers were identified as well as the oxygen vacancy center E_1'. All these centers have been previously observed in both laboratory irradiated artificial and natural quartz and have been associated with α and γ bombardment in the Athabasca basin. Of significance is the absence of peroxy center H_3' from basement quartz as well as its relatively (in comparison to other defects) high concentration in the sandstone. This has been attributed to different growth processes of the quartz.

- Blue, milky and clear quartz types were found lacking in α related defects with blue grains from the psammo-pelitic basement recording the lowest values. Highest intensities were observed in pink quartz with smoky ones being lower but comparable.

- RID concentration was found to increase exponentially relative to its vicinity to mineralization zones although a significant number of samples near (< 20m) these same areas exhibit no defects. This, in addition with blue quartz lacking in defects, confirms the structurally-controlled nature of the U-fluids at Arrow suggesting that a more structure-focused approach is needed when studying basement hosted deposits compared to the unconformity based ones from the eastern Athabascas basin.

- CL analysis of selected samples confirmed the presence of characteristic yellow-orange rims in smoky crystals with high EPR intensities. These rims were observed to be of secondary nature occurring after quartz growth suggesting that smoky quartz occurred during secondary U remobilization and alteration phases. High intensity pink quartz veins were instead lacking in CL rims and patches suggesting a more even distribution of defects within the crystal caused by irradiation during quartz growth connecting this type with the main uranium mineralization event.

- Detrital sandstone intensities were found to be comparatively low and at most of the same order of magnitude as reference drusy quartz from sandstones far from mineralization at McArthur River deposit. Intensities were not constant throughout the samples and it was shown that the more highly irradiated samples coincided with the location of underlying mineralization zones. Because of the suggestion that basinal fluids were deficient in U these patterns were interpreted as U-rich structurally controlled basement fluids spilling into the sandstone. The correspondance

of intensity peaks in relation to underlying mineralization, supports the use of EPR on sandstone as an exploration tool for basement hosted mineralization.

References

[1] Alexandre, P., Kyser, K., Thomas, D., Polito, P., Marlat, J. (2009) Geochronology of unconformity related uranium deposits in the Athabasca Basin, Saskatchewan, Canada and their integration in the evolution of the basin; in Mineralium Deposita, Volume 44, Issue 1, 41-59p.

[2] Ainsworth, G. (2016) Eagle Point and Arrow Zone analogy, digital document, *http* : *//www.nexgenenergy.ca* , NexGen Energy Ltd.,*http* : *//www.nexgenenergy.ca/i/pdf/reports/Eagle − Point − Arrow − Zone − Analogy.pdf*, accessed on the 17/12/2016.

[3] Alessi, A., Agnello, S., Buscarino, G., Pan, Y., Mashkovtsev, R. I. (2014) EPR on Radiation-Induced Defects in SiO2. In Applications of EPR in Radiation Research (pp. 255-295). Springer International Publishing.

[4] Azzoni, C.B., Meinardi, F., Paleari. A. (1994) Trapped-hole centers in neutron-irradiated synthetic quartz. Physical Review B, 49, 91829185.

[5] Boero, M., Pasquarello, A., Sarnthein, J., Car, R. (1997) Structure and hyperfine parameters of E1' centers in α-quartz and vitreous SiO2. Physical Review Letters, 78, 887890.

[6] Botis, S. (2005) Electron-paramagnetic-resonance spectroscopy study of radiation-damage-induced cathodoluminescence in quartz, Athabasca Basin. MSc Thesis, Retrieved from the ecommons USASK website. (Accession ID: etd-09072005-130959)

[7] Botis, S., Nokhrin, S., Pan, Y., Xu, Y, Bonli, T., Sopuck, V. (2005) Natural radiation-induced damage in quartz. I. Correlations between cathodoluminescence colors and paramagnetic defects: Canadian Mineralogist, v. 43, p. 1565–1580.

[8] Botis, S., Pan, Y., Bonli, T., Xu, Y., Zhang, A., Nokhrin, S., Sopuck, V. (2006) Natural radiation-induced damage in quartz. II. Distribution and implications for uranium mineralization in the Athabasca Basin, Saskatchewan, Canada: Canadian Mineralogist, v. 44, p. 1387–1402.

[9] Botis, S., Pan, Y., Nokhrin, S., and Nilges, M.J. (2008) Natural radiation induced damage in quartz. III. A new ozonide radical in drusy quartz from the Athabasca basin, Saskatchewan: Canadian Mineralogist, v. 46, p. 125–138.

[10] Calas, G. (1988) Electron paramagnetic resonance: Reviews in Mineralogy, v. 18, p. 513–571.

[11] Cumming, G.L. and Kristic, D. (1992) The age of unconformity uranium mineralization in the Athabasca Basin, northern Saskatchewan. Can. J. Earth Sci. 29:1623 – 1639

[12] Duin, E. Electron Paramagnetic Resonance Theory, digital document, http://www.auburn.edu/∼duinedu/epr/1_theory.pdf, accessed on the 17/12/2016.

[13] Fayek, M. and Kyser, T.K. (1997) Characterization of multiple fluid-flow events and rare-earth element mobility associated with formation of unconformity-type uranium deposits in the Athabasca basin, Saskatchewan. Can. Mineral. 35, 627-658.

[14] Goreva, J.S., Ma, C., Rossman, G.R. (2001) Fibrous nanoinclusions in massive rose quartz: The origin of rose coloration. American Mineralogist, 86(4), pp.466-472.

[15] Gotze, J., Plotze, M., Habermann, D. (2001) Origin, spectral characteristics and practical applications of the cathodoluminescence in quartz- a review. Mineral. Petrol. 71, 225-250.

[16] Hillacre, S. (2015) Structural analysis and paragenesis of the Arrow uranium deposit, Athabasca Basin, northern Saskatchewan: Implications for controls on mineralization. Unpublished B.Sc. Honours thesis, 70pp.

[17] Hoeve, J. and Sibbald, T.I.I. (1978) On the genesis of Rabbit Lake and other unconformity-type uranium deposits in northern Saskatchewan, Canada. Econ. Geol. 73, 1450- 1473.

[18] Hu, B., Pan, Y., Botis, S., Rogers, B., Kotzer, T., Yeo, G. (2008) Radiation-induced defects in drusy quartz, Athabasca Basin, Canada: A new aid to exploration of uranium deposits: Economic Geology, v. 103, p. 1571– 1580.

[19] Ikeya, M. (1993) New Applications of Electron Paramagnetic Resonance: ESR Dating, Dosimetry, and Spectroscopy.

[20] Jefferson, C.W., Thomas, D.J., Gandhi, S.S., Ramaekers, P., Delaney, G., Brisbin, D., Cutts, C., Portella, P., Olson, K.A. (2007) Unconformity-associated uranium deposits of the Athabasca Basin, Saskatchewan and Alberta: Geological Survey of Canada Bulletin, v. 588, p. 23–67.

[21] Kotzer, T.G. and Kyser, T.K. (1995) Petrogenesis of the Proterozoic Athabasca Basin, northern Saskatchewan, Canada, and its relation to diagenesis, hydrothermal uranium mineralization and paleohydrology. Chem. Geol. 120, 45-89.

[22] Komuro, K., Horicawa, Y., Toyoda, S. (2002) Development of radiation-damage halos in low-quartz: cathodoluminescence measurements after He+ implantation: Mineralogy and Petrology, v. 76, p. 261–266.

[23] LePage, Y., Calvert, L.D, Gabe, E.J. (1980) Parameter variation in lowquartz between 94 and 298K. J. Phys. Chem. Solids, 41, 721

[24] Li, Z., Chi, G., Bethune, K. M. (2016) The effects of basement faults on thermal convection and implications for the formation of unconformity-related uranium deposits in the Athabasca Basin, Canada. Geofluids.

[25] Mashkovtsev, R.I., Scherbakova, M., Solntsev, V.P. (1978) EPR of radiation oxygen hole centers in $\alpha-$quartz: Trudy Instituta Geologii i Geofiziki, Akademiia Nauk SSSR Sibirskoe Otdelenie, v. 385, p. 78–86.

[26] Maschmeyer, D. and Lehmann, G. (1983) New hole centers in natural quartz: Physics and Chemistry of Minerals, v. 10, p. 84–88.

[27] Mathisen, M.B. and Ross, D.A. (2016) Technical Report on the Rook I Property, Saskatchewan, Canada, NI 43-101 Technical Report, available at www.sedar.com.

[28] McGavin, D.G. (1987) Symmetry constraints on EPR spin-Hamiltonian parameters. J Magn Reson 74:19-55

[29] Meunier, J.D., Sellier, E., Pagel, M. (1990) Radiation-damage rims in quartz from uranium-bearing sandstones. J. Sed. Petrol. 60, 53-58.

[30] Morton, R.D. (1978) Cathodoluminescence applied to uranium exploration: Nuclide Spectra, v. 11: 1.

[31] Neuser, R.D., Bruhn, F., G6tze, J., Habermann, D., Richter, D.K. (1995) Cathodoluminescence: Method and application. Zbl. Geol. Pali ont., Teil l, H 112, 287-306.

[32] NexGen Energy Ltd; Skyes, J., Rozdilsky, S.,Kocay, J., Browne, B., Ainsworth, G. (2014) Arrow: A New High-Grade Uranium Discovery In An Emerging District, Presentation, Saskatchewan Geological Survey Open House, http://www.er.gov.sk.ca /adx/aspx/adxGetMedia.aspx?DocID=20343, 20337,20331,11265,11254,3385,5460,2936, Documents&MediaID=10ca112e-8178-4bf7-85e6-ec5946fcc2d6 &Filename=5_Sykes_Open_House_2014.pdf.

[33] NexGen Energy Ltd, Ainsworth, G., McNamara, G., Engdahl, A. (2015) Arrow: A Rapidly Growing Uranium Discovery, Presentation, Saskatchewan Geological Survey Open House, http://publications.gov.sk.ca/details.cfm?p=82534.

[34] NexGen Energy Ltd, Ainsworth, G. (2016) Arrow: The basin's largest undeveloped deposit, Presentation, Saskatchewan Geological Survey Open House, http://www.publications.gov.sk.ca/details.cfm?p=83528.

[35] Nilges, M.J., Pan, Y., Mashkovtsev, R.I. (2008) Radiation-induced defects in quartz. I. Single-crystal W-band EPR study of an electron-irradiated quartz: Physics and Chemistry of Minerals, v. 35, p. 103–115.

[36] Nilges, M., Pan, Y., Mashkovtsev, R. (2009) Radiation-induced defects in quartz. III. Single crystal EPR, ENDOR and ESEEM study of a peroxy radical. Phys Chem Miner 36:61–73

[37] Nuttall, R. H. D. and Weil, J. A. (1981) The magnetic properties of the oxygen-hole aluminum centers in crystalline SiO2. I.[AlO4] 0. Canadian Journal of physics, 59(11), 1696-1708.

[38] Owen, M.R. (1998) Radiation-damage haloes in quartz. Geology 16, 529-532.

[39] Pan, Y., Chen, N., Weil, J.A., Nilges, M.J. (2002) Electron paramagnetic resonance spectroscopic study of synthetic fluorapatite. Part III. Structural characterization of sub-ppm-level Gd and Mn in minerals at W-band frequency. Am Mineral 87:1333-1341

[40] Pan, Y., Botis, S., Nokhrin, S. (2006) Applications of natural radiation-induced paramagnetic defects in quartz to exploration in sedimentary basins: Journal of China University of Geosciences, v. 17, no. 3, p. 258–271.

[41] Pan, Y., Nilges, M.J., Mashkovtsev, R.I., (2008) Radiation- induced defects in quartz. II. W-band single-crystal EPR study of a natural citrine: Physics and Chemistry of Minerals, v. 35, p. 387–397.

[42] Pan, Y., Nilges, M.J., Mashkovtsev, R.I. (2009) Radiation-induced defects in quartz: a multifrequency EPR study and DFT modelling of new peroxy radicals, Mineralogical Magazine, Vol.73(4), pp.519-535

[43] Pan, Y. and Hu, B. (2009) Radiation-induced defects in quartz. IV. Thermal stabilities and implications: Physics and Chemistry of Minerals, v. 36, p. 421–430.

[44] Pan, Y., Yeo, G., Rogers, B., Austman, C., Hu, B. (2013) Application of Radiation-Induced Defects in Quartz to Exploration for Uranium Deposits: A Case Study of the Maw Zone, Athabasca Basin, Saskatchewan; Explor. Mining Geol. v. 21, p. 115-12

[45] Rae, A.D. (1969) Relationship between the Experimental Hamiltonian and the Point Symmetry of a Paramagnetic Species in a Crystal, The Journal of Chemical Physics 50, 2672.

[46] Ramaekers, P., Jefferson, C.W., Yeo, G.M., Collier, B., Long, D.F., Drever, G., McHardy, S., Jiricka, D., Cutts, C., Wheatley, K., Catuneanu, O., Bernier, S., Kupsch, B., Post, R. (2007) Revised geological map and stratigraphy of the Athabasca Group, Saskatchewan and Alberta, in Jefferson, C.W. and Delaney, G., eds., EXTECH IV: Geology and Uranium EXploration TECHnology of the Proterozoic Athabasca Basin, Saskatchewan and Alberta: Geological Survey of Canada, Bulletin 588, p. 155–191.

[47] Ramseyer, K., Baumann, J., Matter, A., Mullis, J. (1988) Cathodoluminescence colours of α-quartz. Mineral. Mag. 52, 669-677.

[48] Rosenberg, P.E. and Foit, F.F. (2006) Magnesiofoitite from the uranium deposits of the Athabasca Basin, Saskatchewan, Canada. The Canadian Mineralogist, 44(4), pp.959-965.

[49] Sawakuchi, G.O, Okuno, E. (2004) Effects of high gamma ray doses in quartz, Nuclear Instruments and Methods in Physics Research Section B: Beam Interactions with Materials and Atoms, Volume 218, Pages 217-221

[50] Silsbee, R.H. (1961) Electron spin resonance in neutronirradiated quartz. Journal of Applied Physics, 32, 14591462.

[51] Toyoda, S., Komuro, K., Sato, K., Ikeya, M., Yoshida, H. (1998) ESR and CL observed in quartz grains from uranium deposits: Implications for uranium migration in natural hydrogeological environments: Radiochimica Acta, v. 82, p. 331–334.

[52] Weeks, R.A. (1956) Paramagnetic resonance of lattice defects in irradiated quartz. Journal of Applied Physics, 27, 1376-1381.

[53] Weil, J.A. and Bolton, J.R. (2007) Electron Paramagnetic Resonance: Elementary Theory and Practical Applications: John Wiley & Sons, Hoboken, New Jersey, 688 p.

[54] Weil, J.A. (1984) A review of electron spin resonance and its applications to the study of paramagnetic defects in crystalline quartz. Physics and Chemistry of Minerals, 10, 149165.

[55] Yeo, G., Jefferson, C., and Ramaekers, P. (2007) Comparison of lower Athabasca Group stratigraphy among depositional systems, Saskatchewan and Alberta, in Jefferson, C.W. and Delaney, G., eds., EXTECH IV: Geology and Uranium EXploration TECHnology of the Proterozoic Athabasca Basin, Saskatchewan and Alberta: Geological Survey of Canada, Bulletin 588, p. 465–488.

[56] Zhang, G., Wasyliuk, K., Pan, Y. (2001) The characterization and quantitative analysis of clay minerals in the Athabasca basin, Saskatchewan: application of shortwave infrared reflectance spectroscopy. Can. Mineral. 39, 1347-1363.

[57] Zinkernagel, U. (1978) Cathodoluminescence of quartz and application to sandstone petrology. Contrib. Sed. 8, 1-69.

Appendices

A Samples collected and analyzed

Sample nomenclature is as follows:

- Arrow: first 3 numbers = hole ID.

  Fourth number = 1 for basement and 2 for sandstone.

  Last 3 numbers = downhole depth.

- Regional: RK = Rook exploration hole, CN = Cannon , BO = Bow.

  First 2 numbers = hole number.

  Last 3 numbers = downhole depth.

sample #	Hole ID	Depth (m)	Quartz type	Location
0201196	AR-14-02	196	Milky	Arrow Deposit
0801635	AR-14-08	635	Pink	Arrow Deposit
1201697	AR-14-12	697	Blue	Arrow Deposit
1601131	AR–14-16	131	Milky	Arrow Deposit
1601405	AR-14-16	405	Milky	Arrow Deposit
1602100	AR-14-16	100	Sandstone	Arrow Deposit
2502096	AR-14-25	96	Sandstone	Arrow Deposit
2602119	AR-14-26	119	Sandstone	Arrow Deposit
2801247	AR-14-28	247	Smoky	Arrow Deposit
2802101	AR-14-28	101	Sandstone	Arrow Deposit
3302160	AR-15-33	160	Sandstone	Arrow Deposit
3501238	AR-15-35	238	Milky	Arrow Deposit
3501238	AR-15-35	238	Smoky	Arrow Deposit
3501238	AR-15-35	238	Pink	Arrow Deposit
3502059	AR-15-35	59	Sandstone	Arrow Deposit
3701290	AR-15-37	290	Milky	Arrow Deposit
3701311	AR-15-37	311	Blue	Arrow Deposit
3701322	AR-15-37	322	Milky	Arrow Deposit
3702123	AR-15-37	123	Sandstone	Arrow Deposit
3801726	AR-15-38	726	Milky	Arrow Deposit
3802124	AR-15-38	124	Sandstone	Arrow Deposit
4002098	AR-15-40	98	Sandstone	Arrow Deposit
4701616	AR-15-47	616	Milky	Arrow Deposit
4701691	AR-15-47	691	Clear	Arrow Deposit
4811240	AR-15-48c1	240	Milky	Arrow Deposit
4821323	AR-15-48c2	323	Milky	Arrow Deposit
4821424	AR-15-48c2	424	Pink	Arrow Deposit
4821428	AR-15-48c2	428	Pink	Arrow Deposit
4821429	AR-15-48c2	429	Pink	Arrow Deposit
4831698	AR-15-48c3	698	Smoky	Arrow Deposit
4831744	AR-15-48c3	744	Milky	Arrow Deposit

4901444	AR-15-49c2	444	Pink	Arrow Deposit
4921681	AR-15-49c2	681	Pink	Arrow Deposit
4921693	AR-15-49c2	693	Pink	Arrow Deposit
5001147	AR-15-50	147	Milky	Arrow Deposit
5001194	AR-15-50	194	Milky	Arrow Deposit
5001243	AR-15-50	243	Pink	Arrow Deposit
5001456	AR-15-50	456	Pink	Arrow Deposit
5001457	AR-15-50	457	Pink	Arrow Deposit
5201716	AR-15-52	716	Smoky	Arrow Deposit
5201717	AR-15-52	717	Smoky	Arrow Deposit
5201732	AR-15-52	732	Clear	Arrow Deposit
5201813	AR-15-52	813	Milky	Arrow Deposit
5311694	AR-15-53	694	Pink	Arrow Deposit
5321387	AR-15-53	387	Pink	Arrow Deposit
5321598	AR-15-53	598	Smoky	Arrow Deposit
5321638	AR-15-53	638	Milky	Arrow Deposit
5411267	AR-15-54c1	267	Blue	Arrow Deposit
5411323	AR-15-54c1	323	Milky	Arrow Deposit
5421757	AR-15-54c2	757	Blue	Arrow Deposit
5421759	AR-15-54c2	759	Clear	Arrow Deposit
5431546	AR-15-54c3	546	Milky	Arrow Deposit
5621427	AR-15-56c2	427	Pink	Arrow Deposit
5621817	AR-15-56c2	817	Clear	Arrow Deposit
5631681	AR-15-56c3	681	Clear	Arrow Deposit
5711313	AR-15-57c1	313	Milky	Arrow Deposit
5711362	AR-15-57c1	362	Pink	Arrow Deposit
5711387	AR-15-57c1	387	Pink	Arrow Deposit
5711425	AR-15-57c1	425	Pink	Arrow Deposit
5711458	AR-15-57c1	458	Smoky	Arrow Deposit
5711458	AR-15-57c1	458	Pink	Arrow Deposit
5721405	AR-15-57c2	405	Pink	Arrow Deposit
5721529	AR-15-57c2	529	Blue	Arrow Deposit
5721741	AR-15-57c2	741	Clear	Arrow Deposit
5721776	AR-15-57c2	776	Clear	Arrow Deposit
5811312	AR-15-58c1	312	Milky	Arrow Deposit
5811402	AR-15-58c1	402	Pink	Arrow Deposit
5811545	AR-15-58c1	545	Clear	Arrow Deposit
5811714	AR-15-58c1	714	Smoky	Arrow Deposit
5811745	AR-15-58c1	745	Pink	Arrow Deposit
5811758	AR-15-58c1	758	Smoky	Arrow Deposit

5811772	AR-15-58c1	772	Blue	Arrow Deposit
5811772	AR-15-58c1	772	Pink	Arrow Deposit
5811780	AR-15-58c1	780	Pink	Arrow Deposit
5811920	AR-15-58c1	920	Blue	Arrow Deposit
5811920	AR-15-58c1	920	Clear	Arrow Deposit
5821505	AR-15-58c2	505	Smoky	Arrow Deposit
5911590	AR-15-59c1	590	Smoky	Arrow Deposit
5911609	AR-15-59c1	609	Blue	Arrow Deposit
5911609	AR-15-59c1	609	Smoky	Arrow Deposit
5921441	AR-15-59c2	441	Smoky	Arrow Deposit
5921811	AR-15-59c2	811	Blue	Arrow Deposit
5921811	AR-15-59c2	811	Pink	Arrow Deposit
5921863	AR-15-59c2	863	Milky	Arrow Deposit
5921875	AR-15-59c2	875	Clear	Arrow Deposit
5921896	AR-15-59c2	896	Clear	Arrow Deposit
8301139	RK-15-83	139	Smoky	Rook I Regional
29a2096	AR-15-29a	96	Sandstone	Arrow Deposit
40b1257	AR-15-40b	257	Milky	Arrow Deposit
43a2108	AR-15-43a	108	Sandstone	Arrow Deposit
44b1179	AR-15-44b	176	Clear	Arrow Deposit
44b1293	AR-15-44b	293	Milky	Arrow Deposit
44b1410	AR-15-44b	410	Clear	Arrow Deposit
44b1793	AR-15-44b	793	Milky	Arrow Deposit
44b1825	AR-15-44b	825	Blue	Arrow Deposit
44b1841	AR-15-44b	841	Milky	Arrow Deposit
44b1988	AR-15-44b	988	Clear	Arrow Deposit
44b2100	AR-15-44b	100	Sandstone	Arrow Deposit
44b2105	AR-15-44b	105	Sandstone	Arrow Deposit
44b2108	AR-15-44b	108	Sandstone	Arrow Deposit
0902094	AR-14-09	94	Sandstone	Arrow Deposit
1002109	AR-14-10	109	Sandstone	Arrow Deposit
1102098	AR-14-11	98	Sandstone	Arrow Deposit
1202098	AR-14-12	98	Sandstone	Arrow Deposit
1302103	AR-14-13	103	Sandstone	Arrow Deposit
1502130	AR-14-15	130	Sandstone	Arrow Deposit
1702108	AR-14-17	108	Sandstone	Arrow Deposit
1802107	AR-14-18	107	Sandstone	Arrow Deposit
1902107	AR-14-19	107	Sandstone	Arrow Deposit
2002104	AR-14-20	104	Sandstone	Arrow Deposit
2102113	AR-14-21	113	Sandstone	Arrow Deposit
2202117	AR-14-22	117	Sandstone	Arrow Deposit

2402120	AR-14-24	120	Sandstone	Arrow Deposit
2702099	AR-14-27	99	Sandstone	Arrow Deposit
3102098	AR-14-31	98	Sandstone	Arrow Deposit
3202102	AR-14-32	102	Sandstone	Arrow Deposit
3402129	AR-15-34	129	Sandstone	Arrow Deposit
3502116	AR-15-35	116	Sandstone	Arrow Deposit
3902106	AR-15-39	106	Sandstone	Arrow Deposit
4102102	AR-15-41	102	Sandstone	Arrow Deposit
5402108	AR-15-54	102	Sandstone	Arrow Deposit
5502103	AR-15-55	103	Sandstone	Arrow Deposit
5602110	AR-15-56	110	Sandstone	Arrow Deposit
5702108	AR-15-57	108	Sandstone	Arrow Deposit
5802101	AR-15-58	101	Sandstone	Arrow Deposit
6102110	AR-15-61	110	Sandstone	Arrow Deposit
6202104	AR-15-62	104	Sandstone	Arrow Deposit
7502101	AR-16-75	101	Sandstone	Arrow Deposit
1602100	AR-14-16	100	Sandstone	Arrow Deposit
2502096	AR-14-25	96	Sandstone	Arrow Deposit
2602119	AR-14-26	119	Sandstone	Arrow Deposit
2802101	AR-14-28	101	Sandstone	Arrow Deposit
3302106	AR-15-33	106	Sandstone	Arrow Deposit
3502059	AR-15-35	59	Sandstone	Arrow Deposit
3702123	AR-15-37	123	Sandstone	Arrow Deposit
3802124	AR-15-38	124	Sandstone	Arrow Deposit
4002098	AR-15-40	98	Sandstone	Arrow Deposit
2902096	AR-15-29	96	Sandstone	Arrow Deposit
4302108	AR-15-43	108	Sandstone	Arrow Deposit
4402108	AR-15-44	108	Sandstone	Arrow Deposit
BO01117	BO-15-01	117	Sandstone	Bow Discovery
BO03102	BO-15-02	102	Sandstone	Bow Discovery
BO04119	BO-15-04	119	Sandstone	Bow Discovery
BO05082	BO-15-05	82	Sandstone	Bow Discovery
BO06114	BO-15-06	114	Sandstone	Bow Discovery
BO07103	BO-15-07	103	Sandstone	Bow Discovery
BO09110	BO-15-09	110	Sandstone	Bow Discovery
BO10120	BO-15-10	120	Sandstone	Bow Discovery
BO11114	BO-15-11	114	Sandstone	Bow Discovery
BO12093	BO-15-12	93	Sandstone	Bow Discovery
BO13123	BO-15-13	123	Sandstone	Bow Discovery
BO14109	BO-15-14	109	Sandstone	Bow Discovery
CN02101	CN-16-02		Sandstone	Cannon Discovery

CN04101	CN-16-04	101	Sandstone	Cannon Discovery
CN05101	CN-16-05	101	Sandstone	Cannon Discovery
CN06103	CN-16-06	103	Sandstone	Cannon Discovery
CN07104	CN-16-07	104	Sandstone	Cannon Discovery
CN08106	CN-16-08	106	Sandstone	Cannon Discovery
CN09103	CN-16-09	103	Sandstone	Cannon Discovery
CN10103	CN-16-10	103	Sandstone	Cannon Discovery
CN11086	CN-16-11	86	Sandstone	Cannon Discovery
RK42084	RK-14-42	84	Sandstone	Rook I Regional
RK52081	RK-15-52	81	Sandstone	Rook I Regional
RK53091	RK-15-53	91	Sandstone	Rook I Regional
RK54094	RK-15-54	94	Sandstone	Rook I Regional
RK56102	RK-15-56	102	Sandstone	Rook I Regional
RK58105	RK-15-58	105	Sandstone	Rook I Regional
RK59099	RK-15-59	99	Sandstone	Rook I Regional
RK61104	RK-15-61	104	Sandstone	Rook I Regional
RK62098	RK-15-62	98	Sandstone	Rook I Regional
RK63096	RK-15-63	96	Sandstone	Rook I Regional
RK64131	RK-15-64	131	Sandstone	Rook I Regional
RK66106	RK-15-66	106	Sandstone	Rook I Regional
RK83071	RK-15-83	71	Sandstone	Rook I Regional
RK72126	RK-15-72	126	Sandstone	Rook I Regional
RK84097	RK-6-84	97	Sandstone	Rook I Regional
RK85096	RK-16-85	96	Sandstone	Rook I Regional
RK87089	RK-16-87	89	Sandstone	Rook I Regional
RK89091	RK-16-89	91	Sandstone	Rook I Regional
RK94089	RK-16-94	89	Sandstone	Rook I Regional
RK95107	RK-16-95	107	Sandstone	Rook I Regional
RK96096	RK-16-96	96	Sandstone	Rook I Regional
RK97115	RK-16-97	115	Sandstone	Rook I Regional

B List of EPR spectra acquired

All EPR data is available in an electronic file.

Sample# / Folder	File name / Microwave power (db)
29a2096	
	15db.par
	15db.spc
	30db.par
	30db.spc
40b1257	
	15db.par
	15db.spc
	30db.par
	30db.spc
43a2108b	
	15db.par
	15db.spc
	15db_2.par
	15db_2.spc
	30db.par
	30db.spc
	30db_2.par
	30db_2.spc
43a2108h	
	15db.par
	15db.spc
	15db_2.par
	15db_2.spc
	30db.par
	30db.spc
	30db_2.par
	30db_2.spc
44b1179	
	15db.par
	15db.spc
	30db.par
	30db.spc
44b1293	
	15db.par
	15db.spc
	30db.par
	30db.spc
44b1364	
	15db.par
	15db.spc
	30db.par
	30db.spc
44b1410	
	15db.par
	15db.spc
	30db.par
	30db.spc
44b1793	
	15db.par
	15db.spc
	30db.par
	30db.spc
44b1825	
	15db.par
	15db.spc
	30db.par
	30db.spc
44b1841	
	15db.par
	15db.spc
	30db.par
	30db.spc
44b1988	
	15db.par
	5db.spc
	0db.par
	30db.spc
44b2100	
	15db.par
	15db.spc
	30db.par
	30db.spc
44b2105	
	15db.par
	15db.spc
	30db.par
	30db.spc
44b2108	
	15db.par
	15db.spc
	30db.par
	30db.spc
201196	
	15db.par
	15db.spc
	30db.par
	30db.spc
801635	
	15db.par
	15db.spc
	30db.par
	30db.spc
1201697	
	15db.par
	15db.spc
	30db.par
	30db.spc
1601131	
	15db.par
	15db.spc
	30db.par
	30db.spc
1601405	
	15db.par
	15db.spc
	30db.par
	30db.spc

1602100	
	15db.par
	15db.spc
	30db.par
	30db.spc
2502096	
	15db.par
	15db.spc
	30db.par
	30db.spc
2602119b	
	15db.par
	15db.spc
	30db.par
	30db.spc
2602119h	
	15db.par
	15db.spc
	30db.par
	30db.spc
2801247	
	15db.par
	15db.spc
	30db.par
	30db.spc
2802101	
	15db.par
	15db.spc
	30db.par
	30db.spc
3302160	
	15db.par
	15db.spc
	30db.par
	30db.spc
3501238p	
	15db.par
	15db.spc
	30db.par
	30db.spc
3501238s	
	15db.par
	15db.spc
	30db.par
	30db.spc
3501238w	
	15db.par
	15db.spc
	30db.par
	30db.spc
3502059b	
	15db.par
	15db.spc
	30db.par
	30db.spc
3502059h	
	15db.par
	15db.spc
	30db.par
	30db.spc

3701290	
	15db.par
	15db.spc
	30db.par
	30db.spc
3701311	
	15db.par
	15db.spc
	30db.par
	30db.spc
3701322	
	15db.par
	15db.spc
	30db.par
	30db.spc
3702123	
	15db.par
	15db.spc
	30db.par
	30db.spc
3801726	
	15db.par
	15db.spc
	30db.par
	30db.spc
3802124	
	15db.par
	15db.spc
	30db.par
	30db.spc
4002098	
	15db.par
	15db.spc
	30db.par
	30db.spc
4701616	
	15db.par
	15db.spc
	30db.par
	30db.spc
4701691	
	15db.par
	15db.spc
	30db.par
	30db.spc
4701725g	
	30db.par
	30db.spc
4701725w	
	15db.par
	15db.spc
	30db.par
	30db.spc
	30dbwide.par
	30dbwide.spc
4811240	
	15db.par
	15db.spc
	30db.par
	30db.spc

4821323
15db.par
15db.spc
30db.par
30db.spc
4821424
15db.par
15db.spc
30db.par
30db.spc
4821428
15db.par
15db.spc
30db.par
30db.spc
4821429
15db.par
15db.spc
30db.par
30db.spc
4831698
15db.par
15db.spc
30db.par
30db.spc
4831744
15db.par
15db.spc
30db.par
30db.spc
4901444
15db.par
15db.spc
30db.par
30db.spc
4921681
15db.par
15db.spc
30db.par
30db.spc
4921693
15db.par
15db.spc
30db.par
30db.spc
5001147
15db.par
15db.spc
30db.par
30db.spc
5001194
15db.par
15db.spc
30db.par
30db.spc
5001243
15db.par
15db.spc
30db.par
30db.spc

5001456
15db.par
15db.spc
30db.par
30db.spc
5001457
15db.par
15db.spc
30db.par
30db.spc
5201716
15db.par
15db.spc
30db.par
30db.spc
5201717
15db.par
15db.spc
20db.par
20db.spc
25db.par
25db.spc
30db.par
30db.spc
5201732
15db.par
15db.spc
30db.par
30db.spc
5201813
15db.par
15db.spc
30db.par
30db.spc
5311694bk
50db.par
50db.spc
50dbwide.par
50dbwide.spc
5311694g
15db.par
15db.spc
30db.par
30db.spc
5321387
15db.par
15db.spc
30db.par
30db.spc
5321598
15db.par
15db.spc
30db.par
30db.spc
5321638
15db.par
15db.spc
30db.par
30db.spc

5411267
15db.par
15db.spc
30db.par
30db.spc
5411323
15db.par
15db.spc
30db.par
30db.spc
5421757
15db.par
15db.spc
30db.par
30db.spc
5421759
15db.par
15db.spc
30db.par
30db.spc
5421805
30db.par
30db.spc
30dbwide.par
30dbwide.spc
5431546
15db.par
15db.spc
30db.par
30db.spc
5621427
15db.par
15db.spc
30db.par
30db.spc
5621817
15db.par
15db.spc
30db.par
30db.spc
5631681
15db.par
15db.spc
30db.par
30db.spc
5711313
15db.par
15db.spc
30db.par
30db.spc
5711362
15db.par
15db.spc
30db.par
30db.spc
5711387
15db.par
15db.spc
30db.par
30db.spc

5711425
15db.par
15db.spc
30db.par
30db.spc
5711458g
15db.par
15db.spc
30db.par
30db.spc
5711458p
15db.par
15db.spc
30db.par
30db.spc
5721405
15db.par
15db.spc
30db.par
30db.spc
5721529
15db.par
15db.spc
30db.par
30db.spc
5721741
15db.par
15db.spc
30db.par
30db.spc
5721776
15db.par
15db.spc
30db.par
30db.spc
5811312
15db.par
15db.spc
30db.par
30db.spc
5811402
15db.par
15db.spc
30db.par
30db.spc
5811545
15db.par
15db.spc
30db.par
30db.spc
5811714
15db.par
15db.spc
30db.par
30db.spc
5811745
15db.par
15db.spc
15dbwide.par
15dbwide.spc
30db.par
30db.spc

5811758	
	15db.par
	15db.spc
	30db.par
	30db.spc
5811758bis	
	15db.par
	15db.spc
	30db.par
	30db.spc
5811772b	
	15db.par
	15db.spc
	30db.par
	30db.spc
5811772p	
	15db.par
	15db.spc
	30db.par
	30db.spc
5811780	
	15db.par
	15db.spc
	30db.par
	30db.spc
5811920b	
	15db.par
	15db.spc
	30db.par
	30db.spc
5811920bw	
	30db.par
	30db.spc
5811920ss	
	30db.par
	30db.spc
5811920ts	
	15db.par
	15db.spc
	30db.par
	30db.spc
5811920ts2	
	30db.par
	30db.spc
5821505	
	15db.par
	15db.spc
	30db.par
	30db.spc
5911590	
	15db.par
	15db.spc
	30db.par
	30db.spc
5911609b	
	15db.par
	15db.spc
	30db.par
	30db.spc
5911609g	
	15db.par
	15db.spc
	30db.par
	30db.spc
5921441	
	15db.par
	15db.spc
	30db.par
	30db.spc
5921811b	
	15db.par
	15db.spc
	30db.par
	30db.spc
5921811g	
	15db.par
	15db.spc
	30db.par
	30db.spc
5921863	
	15db.par
	15db.spc
	30db.par
	30db.spc
5921875	
	15db.par
	15db.spc
	30db.par
	30db.spc
5921896	
	15db.par
	15db.spc
	30db.par
	30db.spc
8301139	
	15db.par
	15db.spc
	30db.par
	30db.spc
mac121_65	
	15db.par
	15db.spc
	30db.par
	30db.spc
mac121_95	
	15db.par
	15db.spc
	30db.par
	30db.spc
mac121_345	
	15db.par
	15db.spc
	30db.par
	30db.spc
mac204_176_1	
	15db.par
	15db.spc
	30db.par
	30db.spc
mac204_421	
	15db.par
	15db.spc
	30db.par
	30db.spc

0902094	
	15db.par
	15db.spc
	30db.par
	30db.spc
1002109	
	15db.par
	15db.spc
	30db.par
	30db.spc
1102098	
	15db.par
	15db.spc
	30db.par
	30db.spc
1202098	
	15db.par
	15db.spc
	30db.par
	30db.spc
1302103	
	15db.par
	15db.spc
	30db.par
	30db.spc
1502130	
	15db.par
	15db.spc
	30db.par
	30db.spc
1702108	
	15db.par
	15db.spc
	30db.par
	30db.spc
1802017	
	15db.par
	15db.spc
	30db.par
	30db.spc
1902107	
	15db.par
	15db.spc
	30db.par
	30db.spc
2002104	
	15db.par
	15db.spc
	30db.par
	30db.spc
2102113	
	15db.par
	15db.spc
	30db.par
	30db.spc
2202117	
	15db.par
	15db.spc
	30db.par
	30db.spc

2402120	
	15db.par
	15db.spc
	30db.par
	30db.spc
2702099	
	15db.par
	15db.spc
	30db.par
	30db.spc
3102098	
	15db.par
	15db.spc
	30db.par
	30db.spc
3202102	
	15db.par
	15db.spc
	30db.par
	30db.spc
3402129	
	15db.par
	15db.spc
	30db.par
	30db.spc
3502116	
	15db.par
	15db.spc
	30db.par
	30db.spc
3902106	
	15db.par
	15db.spc
	30db.par
	30db.spc
4102109	
	15db.par
	15db.spc
	30db.par
	30db.spc
5402108	
	15db.par
	15db.spc
	30db.par
	30db.spc
5502103	
	15db.par
	15db.spc
	30db.par
	30db.spc
5602110	
	15db.par
	15db.spc
	30db.par
	30db.spc
5702108	
	15db.par
	15db.spc
	30db.par
	30db.spc

5802101	
	15db.par
	15db.spc
	30db.par
	30db.spc
6102110	
	15db.par
	15db.spc
	30db.par
	30db.spc
6202104	
	15db.par
	15db.spc
	30db.par
	30db.spc
7502101	
	15db.par
	15db.spc
	30db.par
	30db.spc
Bo01117	
	15db.par
	15db.spc
	30db.par
	30db.spc
bo03102	
	15db.par
	15db.spc
	30db.par
	30db.spc
bo04119	
	15db.par
	15db.spc
	30db.par
	30db.spc
bo05082	
	15db.par
	15db.spc
	30db.par
	30db.spc
bo06114	
	15db.par
	15db.spc
	30db.par
	30db.spc
bo07103	
	15db.par
	15db.spc
	30db.par
	30db.spc
bo09110	
	15db.par
	15db.spc
	30db.par
	30db.spc
bo10120	
	15db.par
	15db.spc
	30db.par
	30db.spc

bo11114	
	15db.par
	15db.spc
	30db.par
	30db.spc
bo12093	
	15db.par
	15db.spc
	30db.par
	30db.spc
bo13123	
	15db.par
	15db.spc
	30db.par
	30db.spc
bo14109	
	15db.par
	15db.spc
	30db.par
	30db.spc
cn02101	
	15db.par
	15db.spc
	30db.par
	30db.spc
cn03091	
	15db.par
	15db.spc
	30db.par
	30db.spc
cn04101	
	15db.par
	15db.spc
	30db.par
	30db.spc
cn05101	
	15db.par
	15db.spc
	30db.par
	30db.spc
cn06103	
	15db.par
	15db.spc
	30db.par
	30db.spc
cn07104	
	15db.par
	15db.spc
	30db.par
	30db.spc
cn08106	
	15db.par
	15db.spc
	30db.par
	30db.spc
cn09103	
	15db.par
	15db.spc
	30db.par
	30db.spc

cn10103	
	15db.par
	15db.spc
	30db.par
	30db.spc
cn11086	
	15db.par
	15db.spc
	30db.par
	30db.spc
rk15094	
	15db.par
	15db.spc
	30db.par
	30db.spc
rk42084	
	15db.par
	15db.spc
	30db.par
	30db.spc
rk52081	
	15db.par
	15db.spc
	30db.par
	30db.spc
rk53091	
	15db.par
	15db.spc
	30db.par
	30db.spc
rk56102	
	15db.par
	15db.spc
	30db.par
	30db.spc
rk59099	
	15db.par
	15db.spc
	30db.par
	30db.spc
rk61114	
	15db.par
	15db.spc
	30db.par
	30db.spc
rk62098	
	15db.par
	15db.spc
	30db.par
	30db.spc
rk63096	
	15db.par
	15db.spc
	30db.par
	30db.spc
rk64131	
	15db.par
	15db.spc
	30db.par
	30db.spc
rk66106	
	15db.par
	15db.spc
	30db.par
	30db.spc
rk72126	
	15db.par
	15db.spc
	30db.par
	30db.spc
rk83071	
	15db.par
	15db.spc
	30db.par
	30db.spc
rk84097	
	15db.par
	15db.spc
	30db.par
	30db.spc
rk85096	
	15db.par
	15db.spc
	30db.par
	30db.spc
rk87089	
	15db.par
	15db.spc
	30db.par
	30db.spc
rk89091	
	15db.par
	15db.spc
	30db.par
	30db.spc
rk94089	
	15db.par
	15db.spc
	30db.par
	30db.spc
rk95107	
	15db.par
	15db.spc
	30db.par
	30db.spc
rk96096	
	15db.par
	15db.spc
	30db.par
	30db.spc
rk96115	
	15db.par
	15db.spc
	30db.par
	30db.spc
rk97115	
	15db.par
	15db.spc
	30db.par
	30db.spc
rk582105	
	15db.par
	15db.spc
	30db.par
	30db.spc

neutron irradiation/basement	
	15dbannealed.par
	15dbannealed.scp
	15dbirradiated.par
	15dbirradiated.scp
	30dbannealed.par
	30dbannealed.scp
	30dbirradiated.par
	30dbirradiated.scp
neutron irradiation/sandstone	
	15dbannealed.par
	15dbannealed.scp
	15dbirradiated.par
	15dbirradiated.scp
	30dbannealed.par
	30dbannealed.scp
	30dbirradiated.par
	30dbirradiated.scp
reference/mac-121-65	
	15db.par
	15db.spc
	30db.par
	30db.spc
reference/mac121-95	
	15db.par
	15db.spc
	30db.par
	30db.spc
reference/mac-121-345	
	15db.par
	15db.spc
	30db.par
	30db.spc
reference/mac204-176-1	
	15db.par
	15db.spc
	30db.par
	30db.spc
reference/mac204-421	
	15db.par
	15db.spc
	30db.par
	30db.spc
reference/WR245-340m	
	15db.par
	15db.spc
	30db.par
	30db.spc
reference/WR245-376m	
	15db.par
	15db.spc
	30db.par
	30db.spc
reference/ZK2-512m	
	15db.par
	15db.spc
	30db.par
	30db.spc
reference/zq15-135m	
	15db.par
	15db.spc
	30db.par
	30db.spc
reference/zq15-135.9m	
	15db.par
	15db.spc
	30db.par
	30db.spc
reference/zq19-335m	
	15db.par
	15db.spc
	30db.par
	30db.spc
reference/zq94-124m	
	15db.par
	15db.spc
	30db.par
	30db.spc

C List of CL spectra and images

Sample	file
2801247	
	DC-2801247-1blue-15kV-0,2mA-150-4x-5s-after30s_1.txt
	DC-2801247-1blue-15kV-0,2mA-150-4x-5s-after60s_1.txt
	DC-2801247-1blue-15kV-0,2mA-150-4x-5s-after120s_1.txt
	DC-2801247-1blue-15kV-0,2mA-150-4x-5s-after180s_1.txt
	DC-2801247-1blue-15kV-0,2mA-150-4x-5s-after240s_1.txt
	DC-2801247-1blue-15kV-0,2mA-150-4x-5s-after300s.xls
	DC-2801247-1blue-15kV-0,2mA-150-4x-5s-after300s_1.txt
	DC-2801247-1blue-15kV-0,2mA-150-4x-5s-beide.xls
	DC-2801247-1blue-15kV-0,2mA-150-4x-5s-initial.xls
	DC-2801247-1blue-15kV-0,2mA-150-4x-5s-initial_1.txt
	DC-2801247-1-KL-4-15safter300s.tif
	DC-2801247-1-KL-4-15sinitial.tif
	DC-2801247-1-n-4.tif
	DC-2801247-1-Pol-4.tif
	DC-2801247-1yellowrim-15kV-0,2mA-150-4x-5s.xls
	DC-2801247-1yellowrim-15kV-0,2mA-150-4x-5s_1.txt
	DC-2801247-2-KL-4-15sinitial.tif
	DC-2801247-2-n-4.tif
	DC-2801247-2-Pol-4.tif
	DC-2801247-3-KL-4-15sinitial.tif
	DC-2801247-3-n-4.tif
	DC-2801247-3-Pol-4.tif
4831698	
	DC-4831698-1blue-15kV-0,2mA-150-4x-5s-after30s_1.txt
	DC-4831698-1blue-15kV-0,2mA-150-4x-5s-after60s_1.txt
	DC-4831698-1blue-15kV-0,2mA-150-4x-5s-after120s_1.txt
	DC-4831698-1blue-15kV-0,2mA-150-4x-5s-after180s_1.txt
	DC-4831698-1blue-15kV-0,2mA-150-4x-5s-after240s_1.txt
	DC-4831698-1blue-15kV-0,2mA-150-4x-5s-after300s.xls
	DC-4831698-1blue-15kV-0,2mA-150-4x-5s-after300s_1.txt
	DC-4831698-1blue-15kV-0,2mA-150-4x-5s-beide.xls
	DC-4831698-1blue-15kV-0,2mA-150-4x-5s-initial.xls
	DC-4831698-1blue-15kV-0,2mA-150-4x-5s-initial_1.txt
	DC-4831698-1-KL-4-10safter30s.tif
	DC-4831698-1-KL-4-13safter300s.tif
	DC-4831698-1-KL-4-13sinitial.tif
	DC-4831698-1-n-4.tif
	DC-4831698-1-Pol-4.tif
	DC-4831698-1yellowrim-15kV-0,2mA-150-4x-5s.xls
	DC-4831698-1yellowrim-15kV-0,2mA-150-4x-5s_1.txt
	DC-4831698-2-KL-4-20sinitial.tif
	DC-4831698-2-n-4.tif
	DC-4831698-2-Pol-4.tif
5001243	
	DC-5001243-1blue-15kV-0,2mA-150-4x-5s-after15s_1.txt
	DC-5001243-1blue-15kV-0,2mA-150-4x-5s-after30s_1.txt
	DC-5001243-1blue-15kV-0,2mA-150-4x-5s-after60s_1.txt
	DC-5001243-1blue-15kV-0,2mA-150-4x-5s-after120s_1.txt
	DC-5001243-1blue-15kV-0,2mA-150-4x-5s-after180s_1.txt
	DC-5001243-1blue-15kV-0,2mA-150-4x-5s-after240s_1.txt
	DC-5001243-1blue-15kV-0,2mA-150-4x-5s-after300s.xls
	DC-5001243-1blue-15kV-0,2mA-150-4x-5s-after300s_1.txt
	DC-5001243-1blue-15kV-0,2mA-150-4x-5s-beide.xls
	DC-5001243-1blue-15kV-0,2mA-150-4x-5s-initial.xls
	DC-5001243-1blue-15kV-0,2mA-150-4x-5s-initial_1.txt
	DC-5001243-1-KL-4-10safter600s.tif

	DC-5001243-1-KL-4-10sinitial.tif
	DC-5001243-1-n-4.tif
	DC-5001243-1-Pol-4.tif
5201716	
	DC-5201716-1blue-15kV-0,2mA-150-4x-5s-after30s_1.txt
	DC-5201716-1blue-15kV-0,2mA-150-4x-5s-after60s_1.txt
	DC-5201716-1blue-15kV-0,2mA-150-4x-5s-after120s_1.txt
	DC-5201716-1blue-15kV-0,2mA-150-4x-5s-after180s_1.txt
	DC-5201716-1blue-15kV-0,2mA-150-4x-5s-after240s_1.txt
	DC-5201716-1blue-15kV-0,2mA-150-4x-5s-after300s.xls
	DC-5201716-1blue-15kV-0,2mA-150-4x-5s-after300s_1.txt
	DC-5201716-1blue-15kV-0,2mA-150-4x-5s-beide.xls
	DC-5201716-1blue-15kV-0,2mA-150-4x-5s-initial.xls
	DC-5201716-1blue-15kV-0,2mA-150-4x-5s-initial_1.txt
	DC-5201716-1-KL-4-15s-after300s.tif
	DC-5201716-1-KL-4-15s-initial.tif
	DC-5201716-1-n-4.tif
	DC-5201716-1-Pol-4.tif
	DC-5201716-2blue-15kV-0,2mA-150-4x-5s-initial_1.txt
	DC-5201716-2-KL-4-15sinitial.tif
	DC-5201716-2-n-4.tif
	DC-5201716-2-Pol-4.tif
	DC-5201716-3blue-15kV-0,2mA-150-4x-5s-after30s_1.txt
	DC-5201716-3blue-15kV-0,2mA-150-4x-5s-after60s_1.txt
	DC-5201716-3blue-15kV-0,2mA-150-4x-5s-after120s_1.txt
	DC-5201716-3blue-15kV-0,2mA-150-4x-5s-after180s_1.txt
	DC-5201716-3blue-15kV-0,2mA-150-4x-5s-after240s_1.txt
	DC-5201716-3blue-15kV-0,2mA-150-4x-5s-after300s.xls
	DC-5201716-3blue-15kV-0,2mA-150-4x-5s-after300s_1.txt
	DC-5201716-3blue-15kV-0,2mA-150-4x-5s-beide.xls
	DC-5201716-3blue-15kV-0,2mA-150-4x-5s-initial.xls
	DC-5201716-3blue-15kV-0,2mA-150-4x-5s-initial_1.txt
	DC-5201716-3-KL-4-15safter300s.tif
	DC-5201716-3-KL-4-15sinitial.tif
	DC-5201716-3-n-4.tif
	DC-5201716-3-Pol-4.tif
5201717	
	DC-5201717-1blue-15kV-0,2mA-150-4x-5s-after30s_1.txt
	DC-5201717-1blue-15kV-0,2mA-150-4x-5s-after60s_1.txt
	DC-5201717-1blue-15kV-0,2mA-150-4x-5s-after120s_1.txt
	DC-5201717-1blue-15kV-0,2mA-150-4x-5s-after180s_1.txt
	DC-5201717-1blue-15kV-0,2mA-150-4x-5s-after240s_1.txt
	DC-5201717-1blue-15kV-0,2mA-150-4x-5s-after300s.xls
	DC-5201717-1blue-15kV-0,2mA-150-4x-5s-after300s_1.txt
	DC-5201717-1blue-15kV-0,2mA-150-4x-5s-beide.xls
	DC-5201717-1blue-15kV-0,2mA-150-4x-5s-initial.xls
	DC-5201717-1blue-15kV-0,2mA-150-4x-5s-initial_1.txt
	DC-5201717-1-KL-4-15safter300s.tif
	DC-5201717-1-KL-4-15sinitial.tif
	DC-5201717-1-n-4.tif
	DC-5201717-1-Pol-4.tif
5711387	
	DC-5711387-1para-KL-4-20safter300s.tif
	DC-5711387-1para-KL-4-20sinitial.tif
	DC-5711387-1para-KL-4-30safter300s.tif
	DC-5711387-1para-n-4.tif
	DC-5711387-1para-Pol-4.tif
	DC-5711387-1perp-15kV-0,2mA-150-4x-5s-after60s_1.txt
	DC-5711387-1perp-15kV-0,2mA-150-4x-5s-after120s_1.txt
	DC-5711387-1perp-15kV-0,2mA-150-4x-5s-after180s_1.txt
	DC-5711387-1perp-15kV-0,2mA-150-4x-5s-after240s_1.txt
	DC-5711387-1perp-15kV-0,2mA-150-4x-5s-after300s.xls

	DC-5001243-1-KL-4-10sinitial.tif
	DC-5001243-1-n-4.tif
	DC-5001243-1-Pol-4.tif
5201716	
	DC-5201716-1blue-15kV-0,2mA-150-4x-5s-after30s_1.txt
	DC-5201716-1blue-15kV-0,2mA-150-4x-5s-after60s_1.txt
	DC-5201716-1blue-15kV-0,2mA-150-4x-5s-after120s_1.txt
	DC-5201716-1blue-15kV-0,2mA-150-4x-5s-after180s_1.txt
	DC-5201716-1blue-15kV-0,2mA-150-4x-5s-after240s_1.txt
	DC-5201716-1blue-15kV-0,2mA-150-4x-5s-after300s.xls
	DC-5201716-1blue-15kV-0,2mA-150-4x-5s-after300s_1.txt
	DC-5201716-1blue-15kV-0,2mA-150-4x-5s-beide.xls
	DC-5201716-1blue-15kV-0,2mA-150-4x-5s-initial.xls
	DC-5201716-1blue-15kV-0,2mA-150-4x-5s-initial_1.txt
	DC-5201716-1-KL-4-15s-after300s.tif
	DC-5201716-1-KL-4-15s-initial.tif
	DC-5201716-1-n-4.tif
	DC-5201716-1-Pol-4.tif
	DC-5201716-2blue-15kV-0,2mA-150-4x-5s-initial_1.txt
	DC-5201716-2-KL-4-15sinitial.tif
	DC-5201716-2-n-4.tif
	DC-5201716-2-Pol-4.tif
	DC-5201716-3blue-15kV-0,2mA-150-4x-5s-after30s_1.txt
	DC-5201716-3blue-15kV-0,2mA-150-4x-5s-after60s_1.txt
	DC-5201716-3blue-15kV-0,2mA-150-4x-5s-after120s_1.txt
	DC-5201716-3blue-15kV-0,2mA-150-4x-5s-after180s_1.txt
	DC-5201716-3blue-15kV-0,2mA-150-4x-5s-after240s_1.txt
	DC-5201716-3blue-15kV-0,2mA-150-4x-5s-after300s.xls
	DC-5201716-3blue-15kV-0,2mA-150-4x-5s-after300s_1.txt
	DC-5201716-3blue-15kV-0,2mA-150-4x-5s-beide.xls
	DC-5201716-3blue-15kV-0,2mA-150-4x-5s-initial.xls
	DC-5201716-3blue-15kV-0,2mA-150-4x-5s-initial_1.txt
	DC-5201716-3-KL-4-15safter300s.tif
	DC-5201716-3-KL-4-15sinitial.tif
	DC-5201716-3-n-4.tif
	DC-5201716-3-Pol-4.tif
5201717	
	DC-5201717-1blue-15kV-0,2mA-150-4x-5s-after30s_1.txt
	DC-5201717-1blue-15kV-0,2mA-150-4x-5s-after60s_1.txt
	DC-5201717-1blue-15kV-0,2mA-150-4x-5s-after120s_1.txt
	DC-5201717-1blue-15kV-0,2mA-150-4x-5s-after180s_1.txt
	DC-5201717-1blue-15kV-0,2mA-150-4x-5s-after240s_1.txt
	DC-5201717-1blue-15kV-0,2mA-150-4x-5s-after300s.xls
	DC-5201717-1blue-15kV-0,2mA-150-4x-5s-after300s_1.txt
	DC-5201717-1blue-15kV-0,2mA-150-4x-5s-beide.xls
	DC-5201717-1blue-15kV-0,2mA-150-4x-5s-initial.xls
	DC-5201717-1blue-15kV-0,2mA-150-4x-5s-initial_1.txt
	DC-5201717-1-KL-4-15safter300s.tif
	DC-5201717-1-KL-4-15sinitial.tif
	DC-5201717-1-n-4.tif
	DC-5201717-1-Pol-4.tif
5711387	
	DC-5711387-1para-KL-4-20safter300s.tif
	DC-5711387-1para-KL-4-20sinitial.tif
	DC-5711387-1para-KL-4-30safter300s.tif
	DC-5711387-1para-n-4.tif
	DC-5711387-1para-Pol-4.tif
	DC-5711387-1perp-15kV-0,2mA-150-4x-5s-after60s_1.txt
	DC-5711387-1perp-15kV-0,2mA-150-4x-5s-after120s_1.txt
	DC-5711387-1perp-15kV-0,2mA-150-4x-5s-after180s_1.txt
	DC-5711387-1perp-15kV-0,2mA-150-4x-5s-after240s_1.txt
	DC-5711387-1perp-15kV-0,2mA-150-4x-5s-after300s.xls
	DC-5711387-1perp-15kV-0,2mA-150-4x-5s-after300s_1.txt

	DC-5711387-1perp-15kV-0,2mA-150-4x-5s-beide.xls
	DC-5711387-1perp-15kV-0,2mA-150-4x-5s-initial.xls
	DC-5711387-1perp-15kV-0,2mA-150-4x-5s-initial_1.txt
	DC-5711387-1perp-KL-4-15sinitial.tif
	DC-5711387-1perp-KL-4-30safter300s.tif
	DC-5711387-1perp-KL-4-30sinitial.tif
	DC-5711387-1perp-n-4.tif
	DC-5711387-1perp-Pol-4.tif
	DC-5711387-2para-15kV-0,2mA-150-4x-5s-after30s_1.txt
	DC-5711387-2para-15kV-0,2mA-150-4x-5s-after60s_1.txt
	DC-5711387-2para-15kV-0,2mA-150-4x-5s-after120s_1.txt
	DC-5711387-2para-15kV-0,2mA-150-4x-5s-after180s_1.txt
	DC-5711387-2para-15kV-0,2mA-150-4x-5s-after300s.xls
	DC-5711387-2para-15kV-0,2mA-150-4x-5s-after300s_1.txt
	DC-5711387-2para-15kV-0,2mA-150-4x-5s-after2400s_1.txt
	DC-5711387-2para-15kV-0,2mA-150-4x-5s-beide.xls
	DC-5711387-2para-15kV-0,2mA-150-4x-5s-initial.xls
	DC-5711387-2para-15kV-0,2mA-150-4x-5s-initial_1.txt
	DC-5711387-3parayellow-15kV-0,2mA-150-4x-5s.xls
	DC-5711387-3parayellow-15kV-0,2mA-150-4x-5s_1.txt
5711425	
	DC-5711425-1blue-15kV-0,2mA-150-4x-5s-after30s_1.txt
	DC-5711425-1blue-15kV-0,2mA-150-4x-5s-after60s_1.txt
	DC-5711425-1blue-15kV-0,2mA-150-4x-5s-after120s_1.txt
	DC-5711425-1blue-15kV-0,2mA-150-4x-5s-after180s_1.txt
	DC-5711425-1blue-15kV-0,2mA-150-4x-5s-after240s_1.txt
	DC-5711425-1blue-15kV-0,2mA-150-4x-5s-after300s.xls
	DC-5711425-1blue-15kV-0,2mA-150-4x-5s-after300s_1.txt
	DC-5711425-1bluecenter-15kV-0,2mA-150-4x-5s-beide.xls
	DC-5711425-1bluecenter-15kV-0,2mA-150-4x-5s-initial.xls
	DC-5711425-1bluecenter-15kV-0,2mA-150-4x-5s-initial_1.txt
	DC-5711425-1bluemargin-15kV-0,2mA-150-4x-5s-initial.xls
	DC-5711425-1bluemargin-15kV-0,2mA-150-4x-5s-initial_1.txt
	DC-5711425-1-KL-4-15safter300s.tif
	DC-5711425-1-KL-4-15sinitial.tif
	DC-5711425-1-n-4.tif
	DC-5711425-1-Pol-4.tif
	DC-5711425-2darkblue-15kV-0,2mA-150-4x-5s.xls
	DC-5711425-2darkblue-15kV-0,2mA-150-4x-5s_1.txt
	DC-5711425-2darkblue-15kV-0,2mA-150-4x-5sboth zones.xls
	DC-5711425-2-KL-4-15sinitial.tif
	DC-5711425-2-n-4.tif
	DC-5711425-2-Pol-4.tif
	DC-5711425-2turq-15kV-0,2mA-150-4x-5s.xls
	DC-5711425-2turq-15kV-0,2mA-150-4x-5s_1.txt
5711458	
	DC-5711458-1blue-15kV-0,2mA-150-4x-5s-after30s_1.txt
	DC-5711458-1blue-15kV-0,2mA-150-4x-5s-after60s_1.txt
	DC-5711458-1blue-15kV-0,2mA-150-4x-5s-after120s_1.txt
	DC-5711458-1blue-15kV-0,2mA-150-4x-5s-after180s_1.txt
	DC-5711458-1blue-15kV-0,2mA-150-4x-5s-after240s_1.txt
	DC-5711458-1blue-15kV-0,2mA-150-4x-5s-after300s.txt
	DC-5711458-1blue-15kV-0,2mA-150-4x-5s-after300s_1.txt
	DC-5711458-1blue-15kV-0,2mA-150-4x-5s-after300s_1.xls
	DC-5711458-1blue-15kV-0,2mA-150-4x-5s-beide.xls
	DC-5711458-1blue-15kV-0,2mA-150-4x-5s-initial.xls
	DC-5711458-1blue-15kV-0,2mA-150-4x-5s-initial_1.txt
	DC-5711458-1-KL-4-10s-after15s.tif
	DC-5711458-1-KL-4-10s-after600s.tif
	DC-5711458-1-KL-4-10s-initial.tif
	DC-5711458-1-n-4.tif
	DC-5711458-1-Pol-4.tif
	DC-5711458-1yellowrim-15kV-0,2mA-150-4x-5s.xls
	DC-5711458-1yellowrim-15kV-0,2mA-150-4x-5s_1.txt